JFM PAPERS

Dynamic characteristic of transonic aeroelasticity affected by fluid mode in pre-buffet flow

Zihao Dou[1]**, Chuanqiang Gao**[1,2,†]** and Weiwei Zhang**[1,2]

[1]School of Aeronautics, Northwestern Polytechnical University, Xi'an 710072, PR China

[2]National Key Laboratory of Aircraft Configuration Design, Xi'an 710072, PR China

Transonic aeroelasticity remains a significant challenge in aerospace. The coupling mechanism of aeroelastic problems involving the coexistence of fluid modes and multiple structural modes still needs further investigation. For this purpose, we analysed the dynamic characteristic of a two-degree-of-freedom (2DOF) NACA0012 airfoil in pre-buffet flow. First, we constructed an aeroelastic reduced-order model, which can represent near-unstable transonic flow using the dominant fluid mode. Then, the flutter mechanism was investigated by studying the main eigenvalues of the model that vary with the natural pitching frequency. The results revealed that the existence of the fluid mode transitions the transonic flutter type from coupled-mode flutter to single-DOF (SDOF) flutter, which leads to a reduction in the flutter boundary. Under the effect of the fluid mode, the system produces six aeroelastic phenomena at different structural natural frequencies, including SDOF heaving/pitching flutter, heaving/pitching instability within coupled-mode flutter, forced vibration and stable state. Moreover, we identified two types of SDOF flutter in the 2DOF system. The first type corresponds to the traditional SDOF flutter, where the coupling of other modes has a small impact on the system's stability in most cases. However, within specific ranges of natural frequencies, this type of SDOF flutter may disappear due to coupling with other modes. The second type of SDOF flutter is characterized by strong coupling dominated by the unstable mode. It arises from the interaction among the flow, heaving and pitching modes, and does not manifest in the absence of any of these modes.

Key words: flow-structure interactions

1. Introduction

Transonic aeroelasticity has always been one of the most challenging issues in the field of aerospace, due to the nonlinearity and instability caused by shock wave motion

and flow separation. Over the years, researchers have extensively investigated transonic aeroelastic problems, covering a range of issues such as transonic flutter (Schewe, Mai & Dietz 2003; Yang *et al.* 2020), transonic buzz (He, Yang & Gu 2016; Halder, Damodaran & Khoo 2020*a*) and transonic buffet (Raveh & Dowell 2011, 2014; Hartmann, Klaas & Schröder 2013). (1) Transonic flutter is mainly caused by coupled-mode flutter, which bears similarities to classical bending–torsion flutter in potential flow (Gao, Liu & Zhang 2021). (2) Transonic buzz (Gao, Zhang & Ye 2016*a*) refers to the self-excited vibration phenomenon of the control surface (rudder or aileron), often resulting in limit-cycle oscillations (LCOs) in a single degree of freedom (SDOF) during flight in transonic or low supersonic flow. (3) Transonic buffet (Bai & Wu 2017) manifests as an aerodynamic phenomenon of self-sustained shock oscillations occurring at a certain combination of Mach number (Ma) and initial angle of attack (AOA). This buffeting flow typically induces forced vibrations in the elastic airfoil, with the oscillation frequency depending on the buffeting frequency. However, the buffet frequency is typically close to the frequency of the first-order structural mode. At this time, by the interaction of buffeting flow and elastic structure, it is found that the oscillation frequency no longer follows the buffet frequency but turns to lock onto the natural frequency of the elastic structure. This special phenomenon is known as frequency lock-in. These classic aeroelastic phenomena collectively demonstrate the intricacies associated with transonic flow (Dowell 2010; Badcock *et al.* 2011; Bendiksen 2011).

In classical flutter, the flow is commonly perceived as an adhesive and dynamic pressure is considered a pivotal parameter for its occurrence. However, the instability characteristics of transonic buzz and frequency lock-in in transonic buffeting differ significantly from those of classical flutter. In these cases, Ma and AOA emerge as primary factors in determining the flutter boundary. In the past, most research focused on the mechanism of transonic buzz arising from negative aerodynamic damping. However, these studies did not explain the reasons for transonic buzz frequently occurring at certain flow states and natural frequencies of the structure. Regarding the phenomenon of frequency lock-in in transonic buffeting, many researchers posit it as a form of nonlinear resonance triggered by shock oscillations. However, the frequency lock-in range extends to twice the buffeting frequency, surpassing the typical range of resonance. This suggests that this explanation does not seem to be reasonable.

In recent studies by Gao *et al.* (2016*a*, 2017*b*), the dominant fluid mode (eigenvalue) is first derived from the linear reduced-order model (ROM) to investigate non-classical aeroelastic phenomena in transonic flow. The coupling mechanisms of transonic buzz and buffet are then explored from the perspective of the fluid mode. Similar to the structural dynamics system, the fluid dynamics system can also be decomposed into several inherent patterns through modal analysis. These inherent patterns encompass modal frequency, damping ratio and modal shape, collectively reflecting the nature of the flow, known as fluid modes (Dowell 2014) (or wake mode; Zhang *et al.* 2015*b*). Generally, the first- to second-order fluid mode can represent the primary characteristics of the flow.

The methods for extracting the essential information about fluid modes can be classified into three main categories: the system identification-based methods (Griffiths *et al.* 2018; Poplingher & Raveh 2023*a*) (including Volterra series, eigensystem realization algorithms and autoregressive with exogenous input (ARX)), the modal decomposition methods (Poplingher, Raveh & Dowell 2019; Halder, Damodaran & Khoo 2020*b*; Shu *et al.* 2023) (such as proper orthogonal decomposition and dynamic mode decomposition (DMD)) and the global stability analysis methods (Sartor, Mettor & Sipp 2015; Paladini *et al.* 2019*a*; Plante *et al.* 2021). Despite the different approaches, the derived dominant fluid
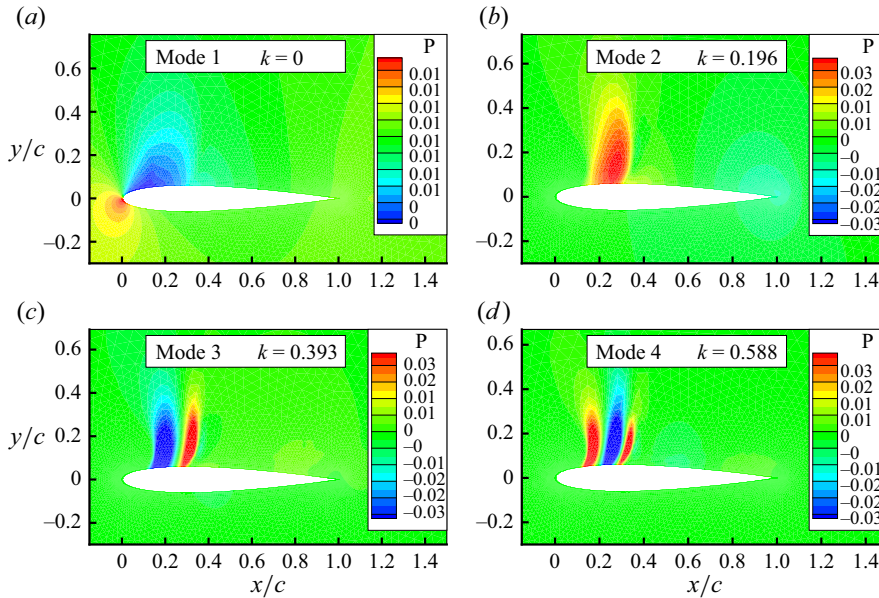
Figure 1. The first four modal shapes of the DMD mode in the buffet case of $Ma = 0.7$, $\alpha = 5.5°$ (Gao *et al.* 2017*a*).

mode essentially remains the same. For instance, the dominant fluid mode is a pair of eigenvalues of the aerodynamic state matrix in the system identification method. The real part of the complex eigenvalue indicates the growth rate (or the damping) of the fluid mode, while the imaginary part indicates the reduced frequency of the dominant fluid mode. For the NACA0012 airfoil in transonic buffeting flow, at $Ma = 0.7$ and $\alpha = 5.5°$, the dimensionless reduced frequency (k) of the fluid mode obtained through the system identification method is 0.2 (Gao & Zhang 2020). This value aligns with the buffet frequency calculated by the computational fluid dynamics (CFD) method and equals the dimensionless frequency of the second mode obtained by the DMD method, as depicted in figure 1. Consequently, this pair of eigenvalues corresponds to the global dominant mode of the transonic buffet flow, dictating the dynamics of the buffet flow system. By the global stability analysis methods, Sartor *et al.* (2015) showed the complete eigenvalue spectrum of the OAT15A airfoil for a wide range of AOA in transonic flow, and found that the buffet phenomenon is driven by an unstable global mode. Paladini *et al.* (2019*b*) used the direct and adjoint unstable global modes to compute the local contribution of the flow to the growth rate and angular frequency of the unstable global mode, and discovered the shock foot is identified as the core of the instability of the transonic buffeting flow field. This purely aerodynamic analysis method is also used to study the link between subsonic stall and transonic buffet on airfoils (Moise, Zauner & Sandham 2024) and wings (Plante *et al.* 2021), and the differences between two-dimensional airfoils and three-dimensional swept wings (Paladini *et al.* 2019*a*).

The fluid mode not only provides an effective means to elucidate the evolution of complex unstable flows but also opens a gateway to understanding the coupling process of the aeroelastic system. The frequency of the fluid mode generally lies in the vicinity of the natural frequencies of the first and second structural modes. This proximity facilitates the coupling between the fluid mode and the structural modes, resulting in a variety of complex aeroelastic phenomena. In the context of blunt body flow,

Kou *et al.* (2017) explained why the lowest Reynolds number (*Re*) for vortex-induced vibration (VIV) to occur is 18 through a ROM-based aeroelastic analysis. A clear and dominant fluid mode emerges from $Re = 18$, becoming unstable at $Re = 47$. When *Re* is lower than 18, it fails to capture a definite fluid mode; thus it is nearly impossible for the fluid system to interact with the elastic structure, and VIV does not happen. Zhang *et al.* (2015*b*) studied the phenomena of the VIV of a circular cylinder, revealing that the frequency lock-in phenomenon at low *Re* can be divided into two patterns according to different induced mechanisms. The two patterns are 'resonance-induced lock-in' and 'flutter-induced lock-in' induced by the fluid mode. Li *et al.* (2019) found that transverse galloping of a square cylinder at low *Re* can be understood as a kind of SDOF flutter induced by the unstable structural mode, superimposed by a forced vibration induced by the unstable fluid mode. Yao & Jaiman (2017) explained the VIV mechanism of square cylinders with different chamfering from the perspective of the fluid mode. From the perspective of coupling and competition between the fluid mode and structural mode, Cheng *et al.* (2023) discovered that very small changes in the windward interior angle of an isosceles-trapezoidal structure can induce or suppress galloping vibrations. For the aeroelastic problems of the airfoil, Moulin & Marquet (2021) studied a two-degree-of-freedom (2DOF) plate in low-Reynolds-number incompressible flows, and revealed four types of unstable modes related to different physical instabilities and classically investigated with separate fluid models: coupled-mode flutter, single-mode flutter, static divergence and vortex-induced vibrations. Gao *et al.* (2016*a*) studied the phenomena of transonic buzz and demonstrated that the instability of the SDOF system is also caused by the coupling of modes: one structural mode and one fluid mode. Gao *et al.* (2017*b*) also indicated that the boundaries and physical mechanism underlying frequency lock-in are caused by linear coupled-mode flutter: the coupling between one structural mode and one fluid mode in unstable buffet flow. Houtman & Timme (2023) conducted research on stability analysis of an elastic wing in transonic flow, and observed that there is no instability in the structural DOF below shock-buffet onset, whereas there are globally unstable fluid modes and additional marginally unstable structural modes that emerge in shock-buffet flow. Korthäuer *et al.* (2023) recently identified the region of the boundaries (Gao *et al.* 2017*b*) of frequency lock-in using experiments, being characterized by the smooth transition from fluid-mode-dominated to structural-mode-dominated coupling. Therefore, the fluid mode offers a new perspective to investigate the physical mechanism of complex aeroelastic problems.

The existing research on the fluid mode has primarily focused on an SDOF aeroelastic system, neglecting the influence of other structural modes. It is critical to fully consider the interaction of the fluid mode with various structural modes, which will enhance the profound comprehension of aeroelastic phenomena in transonic flow. Indeed, there is a well-known classical problem that falls under the category of multi-mode coupling, which is the reduction of the transonic flutter boundary (Isogai 1981; Mallik, Schetz & Kapania 2018; Opgenoord, Drela & Willcox 2018; Gao *et al.* 2021). As early as the 1980s to 1990s, NASA conducted transonic flutter experiments for various standard models, including benchmark active control technology (BACT) (Rivera *et al.* 1992), benchmark supercritical wing (BSCW) (Dansberry *et al.* 1993) and AGARD standard aeroelastic configurations I-wing 445.6 (AGARD445.6) (Yates 1987). It was found that the critical wind speed of transonic flutter decreases, and the flutter frequency gradually synchronizes with the natural frequency of the unstable structural mode as *Ma* or AOA increases. Dowell (2024) and Kholodar *et al.* (2004) conducted a study on transonic flutter of a 2DOF airfoil based on numerical simulation methods, examining the effects of *Ma*, various structural

parameters, etc. This study observed the same phenomenon as in the above experiment and posited that this is an SDOF flutter due to negative aerodynamic damping. This critical aeroelastic mode is still a mass-coupled natural mode, albeit one that is dominated by the unstable structural mode. Over the past decade, the NASA Langley Research Center has spearheaded the organization of three conferences titled the AIAA Aeroelastic Prediction Workshop (AWP) (Schuster *et al.* 2012; Heeg *et al.* 2015; Chwalowski *et al.* 2022). Poplingher & Raveh (2023*b*) presented flutter analysis of the BSCW, at moderate AOA, performed as part of the Third AWP. It was discovered in their studies that, as AOA increases, shock buffet occurs and the flutter mechanism changes from 2DOF to SDOF pitch oscillations. The aforementioned research has established an interaction between transonic flutter and buffet. However, it remains a summary of phenomena, and there has yet to be research conducted from the perspective of the fluid mode. Further research is needed to investigate the impact of the fluid mode on transonic flutter as the AOA/Mach number approaches the buffet boundary. Additionally, the effect of adding other structural modes in the classical transonic buzz problem on the original SDOF flutter needs to be examined.

For this purpose, the present work analysed an aeroelastic system of the 2DOF NACA0012 airfoil in pre-buffet flow (subcritical instability states). While numerical simulations provide acceptable accuracy, they fall short in efficiently analysing the mechanism of aeroelastic problems. Therefore, there is a need for an aeroelastic model that combines high accuracy and efficiency to study the mechanism and dynamic characteristics of transonic aeroelastic problems. In our recent research, the ROM based on ARX was performed in transonic flutter (Gao *et al.* 2021), transonic buzz (Gao *et al.* 2016*a*) and transonic buffet (Gao *et al.* 2017*b*). The efficiency can be improved through the ROM-based method. Firstly, we constructed the ROM-based aeroelastic model by coupling the ARX aerodynamic ROM with the structural motion equations in state space (see § 3). Then, various aeroelastic phenomena under the influence of the transonic fluid mode were identified and analysed for different structural natural frequencies (see § 4). Finally, the results of the ROM-based aeroelastic model were analysed and validated with the CFD and computational structural dynamics (CSD) method (see § 5). The models and the numerical methods are introduced in § 2. Section 6 presents the conclusions.

2. Models and numerical methods

This section presents the methods, models and their correlation employed in the present study. The introduction of the parameters is in § 2.1. The main analysis method is divided into two steps in figure 2.

Step 1. Constructed the ROM-based aeroelastic model. To begin with, we employed a combination of CFD and CSD methods to obtain training data under forced motion. The acquired data were then utilized to construct an unsteady aerodynamic model using system identification techniques. Based on that, we were able to identify and present the dominant fluid mode. Finally, we built the aeroelastic model by coupling the structural model with the unsteady aerodynamic model in the state-space form. The detailed case of unsteady aerodynamic modelling is demonstrated in § 3.1.

Step 2. Analysed the dynamic characteristic of aeroelastic problems affected by the fluid mode. First, the flutter characteristics of the aeroelastic system were analysed using the root loci method under typical frequency ratios, $i_n = k_h/k_\alpha$. Then, we analysed the flutter characteristics and types within the two-dimensional parameter space composed of
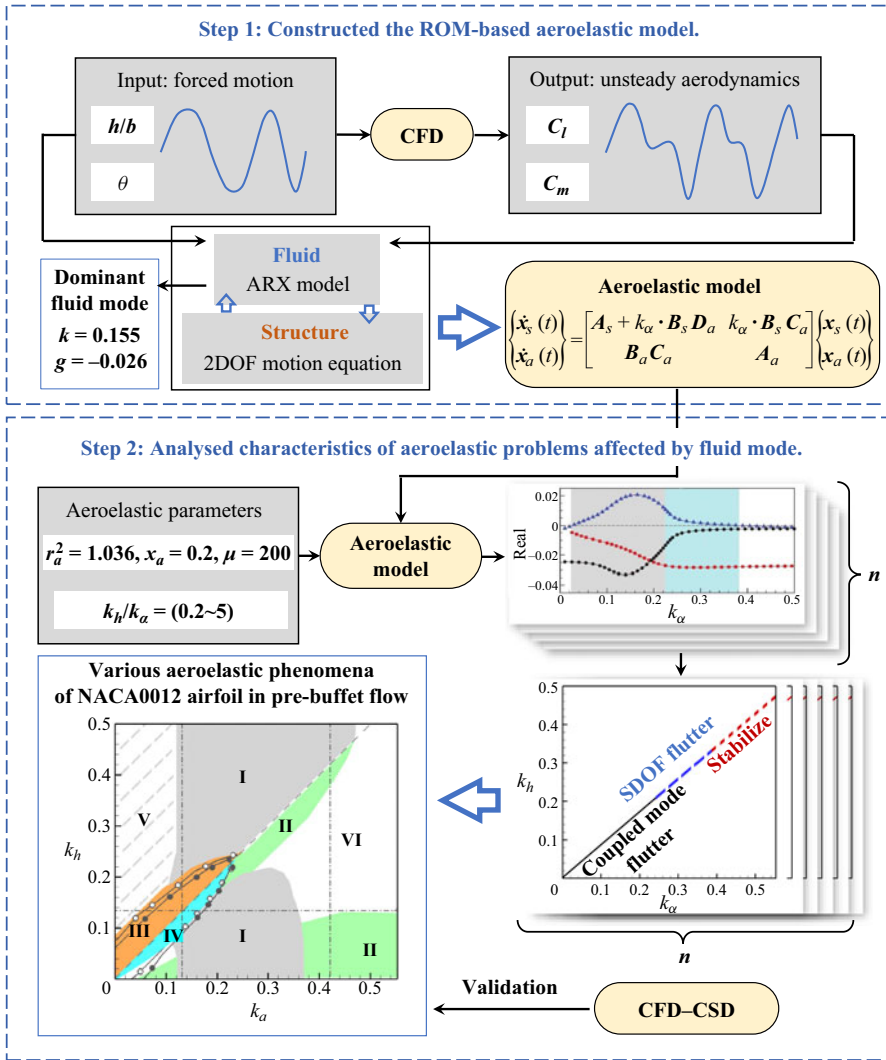
Figure 2. The methods/models used in the present work and their relationship.

k_h and k_α. Finally, mechanism analysis and validation of the typical states were carried out based on numerical simulation methods.

2.1. *The CFD–CSD method*

Through the CFD–CSD method, the data sources and the validation of the aeroelastic model were obtained. The flow analysis was performed by an in-house hybrid-unstructured flow solver using a cell-centred finite volume method to solve unsteady Reynolds-averaged Navier–Stokes (URANS) equations. The integral form of two-dimensional compressible URANS equations with the S-A turbulence model can be written for a cell of volume V limited by a surface S. The equation can be expressed as

$$\frac{\partial}{\partial t} \int_V \boldsymbol{W} \, \mathrm{d}V + \oint_S \boldsymbol{E}^i(\boldsymbol{W}, \boldsymbol{V}_{grid}) \cdot \boldsymbol{n} \, \mathrm{d}S - \oint_S \boldsymbol{E}^v(\boldsymbol{W}) \cdot \boldsymbol{n} \, \mathrm{d}S = \int_V \boldsymbol{H} \, \mathrm{d}V, \qquad (2.1)$$

where $\boldsymbol{n}$ represents the outer unit normal vector to the boundary S; $\boldsymbol{W}$ is a five-component vector of conservative variables, $\boldsymbol{W} = [\rho \, \rho u \, \rho v \, \rho E \, \rho \tilde{v}]^{\mathrm{T}}$, ρ being the density; u, v are x-wise and y-wise components of the velocity vector of the flow; E denotes the specific total energy; $\tilde{v}$ denotes the working variable of the S-A turbulence model; $\boldsymbol{E}^i(\boldsymbol{W}, \boldsymbol{V}_{grid})$ and $\boldsymbol{E}^v(\boldsymbol{W})$ are the inviscid flux and the viscous flux, respectively; and $\boldsymbol{H}$ is the source term.

The spatial discretization and time integration of the turbulence model equation and mean flow equations are carried out in a loosely coupled way. The second-order AUSM+ scheme is conducted to evaluate the inviscid flux, with a reconstruction technique based on the least-squares approach. For high-order reconstruction schemes, the reader is referred to Liu *et al.* (2016). The grid velocity $\boldsymbol{V}_{grid}$ is modified according to the geometric conservation law (Ahn & Kallinderis 2006) when CFD–CSD simulations are performed. The viscous flux term is discretized by the standard central scheme. In the turbulence model, the transport equation for the working variable $\tilde{v}$ is given by the standard form proposed by Spalart & Allmaras (1992). The convective and source terms are discretized by the first-order AUSM+ scheme, and the destruction and diffusion terms by the second-order central scheme in the present study. For unsteady computations, the dual time stepping method, proposed by Jameson (1991), is used to solve the governing equations. At the sub-iteration, the fourth-stage Runge–Kutta scheme is used with local time stepping and residual smoothing to accelerate the convergence.

A no-slip wall boundary condition is applied to the airfoil surface. The location and velocity of the airfoil are updated at each real time step due to the pitching motion of the airfoil. Moreover, the far-field boundary is assigned with a non-reflective boundary condition based on Riemann invariants to ensure that the disturbance generated by the object does not return to the flow field. For more validation of the URANS method, one can refer to our earlier studies (Zhang *et al.* 2015*a*; Gao, Zhang & Ye 2016*b*). The aforementioned partial results are presented in a condensed form in Appendix B.1.

The structural motion equation was used to characterize and solve the elastic deformation of the airfoil. The generalized structural motion equation in matrix form is as follows:

$$\boldsymbol{M}\ddot{\boldsymbol{\xi}} + \boldsymbol{G}\dot{\boldsymbol{\xi}} + \boldsymbol{K}\boldsymbol{\xi} = \boldsymbol{Q}, \qquad (2.2)$$

where $\boldsymbol{\xi}$ is the structural generalized displacement; $\boldsymbol{M}$, $\boldsymbol{G}$ and $\boldsymbol{K}$ are the generalized mass, damping ($\boldsymbol{G} = 0$ in this paper) and stiffness matrix, respectively; and $\boldsymbol{Q}$ is the generalized aerodynamic force provided by the CFD method.

Equation (2.2) can be solved by the fourth-order-accuracy hybrid linear multi-step scheme (Zhang, Jiang & Ye 2007) with a predictor–corrector method. This approach helps to build an efficient, stable and loosely coupled algorithm to perform the CFD-based aeroelastic simulation in the time domain. A previous study (Zhang *et al.* 2007) also investigated the influence of time steps in aeroelastic simulations, indicating that the numerical solution is stable/convergent as long as there are no fewer than 30 time steps in a period. A moving boundary was involved in the simulation of aeroelasticity. Thus, a scheme of computational grid deformation based on the radial basis function interpolation (Wang *et al.* 2015) was employed to match the grid with the new wall boundary condition.

The CFD–CSD method has been applied to the study of transonic flutter (Zhang *et al.* 2015*a*), transonic buzz (Gao *et al.* 2016*a*) and transonic buffeting (Gao *et al.* 2017*b*). Lacking a standard case for the 2DOF buffet, the coupled CFD–CSD simulation method is validated by classical flutter cases with two degrees of freedom. In our previous work,
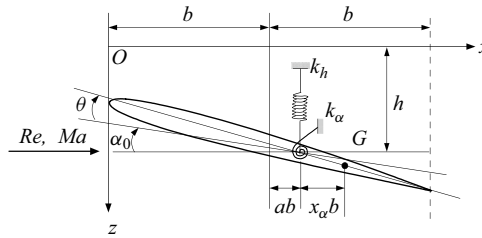
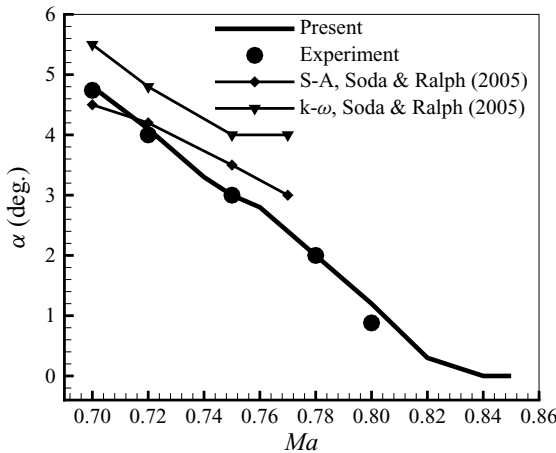Figure 3. Sketch diagram of a 2DOF airfoil system.

Figure 4. Comparison of CFD-calculated buffet boundaries with experimental results at $Ma = 0.7$–0.8 and $Re = 3 \times 10^6$.

flutter boundaries of the BACT model (Zhang *et al.* 2015*a*), the Isogai wing (Zhang *et al.* 2007) and the LCO with NACA64010 airfoil (Zhang *et al.* 2012) agreed well with experimental data and reference results. The aforementioned partial results are presented in a condensed form in Appendix B.3.

2.2. *Aeroelastic case and validation*

The research aeroelastic case is a 2DOF NACA0012 airfoil in subcritical transonic buffeting (pre-buffet) flow, as depicted in figure 3. The free-stream state of the modelling case is $Ma = 0.7$, $Re = 3 \times 10^6$, $\alpha = 4.5°$. The computational hybrid-unstructured mesh has 25 361 nodes, and 40 layers of structured viscous grids around the airfoil, as depicted in figure 48 in Appendix B.2. The time step for the CFD is 3×10^{-4} s (physical), and the non-dimensional time step is 0.1. The convergence of the grid and the time step are presented in Appendix B.2. Figure 4 compares the transonic buffet onset boundary for the NACA0012 airfoil ($Ma = 0.7$–0.8, $Re = 3 \times 10^6$). The circles are from the experiment of Doerffer *et al.* (2010), and the thick solid line is from the URANS method. It also shows the results from Soda & Voss (2005), in which boundaries are larger than those of the experimental data. The experiment and URANS calculations are in satisfactory agreement.

999 A24-8

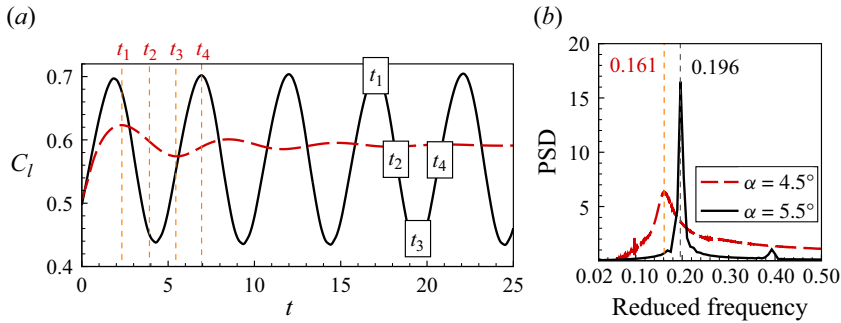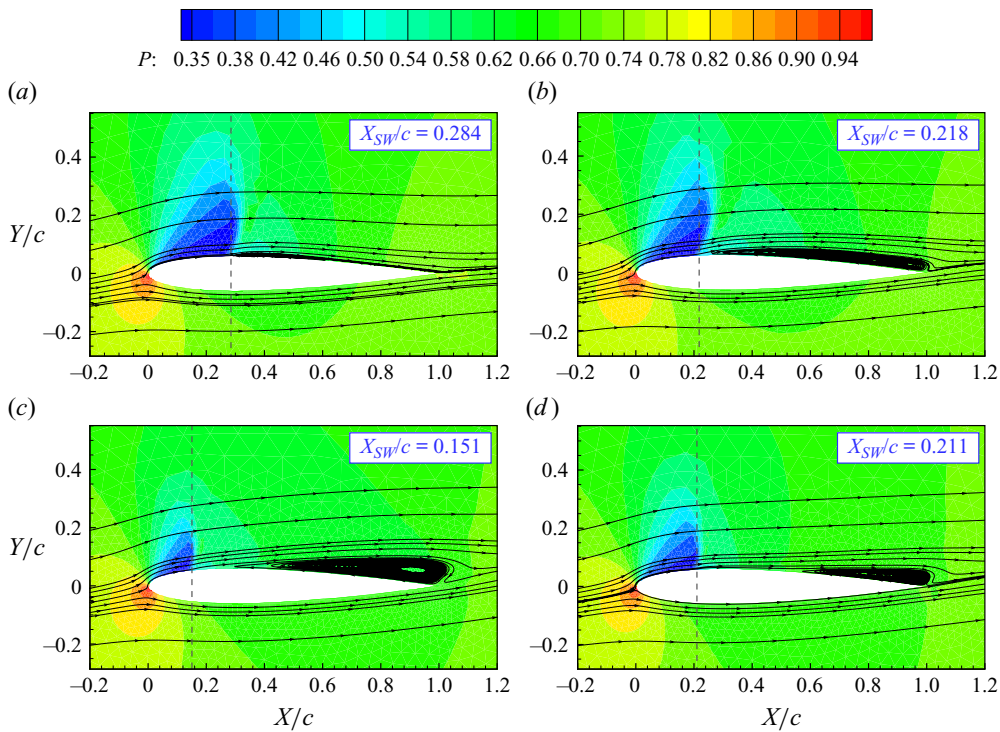Figure 5. The lift responses at $\alpha = 4.5°$ and $\alpha = 5.5°$ at $Ma = 0.7$, and $Re = 3 \times 10^6$.

Figure 6. Pressure contours and streamlines in one period at $\alpha = 5.5°$, $Ma = 0.7$ and $Re = 3 \times 10^6$. Here T is the period of the shock oscillation; X_{SW} is the shock position; and p is the non-dimensional pressure: (a) $t_1 = 0T$, (b) $t_2 = 1/4T$, (c) $t_3 = 1/2T$, (d) $t_4 = 3/4T$.

Angle α is the equilibrium AOA, which is an important parameter affecting the stability of transonic flow, and the stability of the fluid mode is very important for the SDOF flutter. The buffet onset is $4.8°$ for stationary NACA0012 airfoil at $Ma = 0.7$, $Re = 3 \times 10^6$. Time histories of the lift coefficient at $\alpha = 4.5°$ and $\alpha = 5.5°$ are shown in figure 5. It can be seen that dramatic unsteady loads appear at $\alpha = 5.5°$. At $\alpha = 4.5°$, flow oscillates slowly and converges to a stable state after the initial excitation. This indicates that although the flow field is in a subcritical buffeting state, its flow stability margin is not high. Further, the
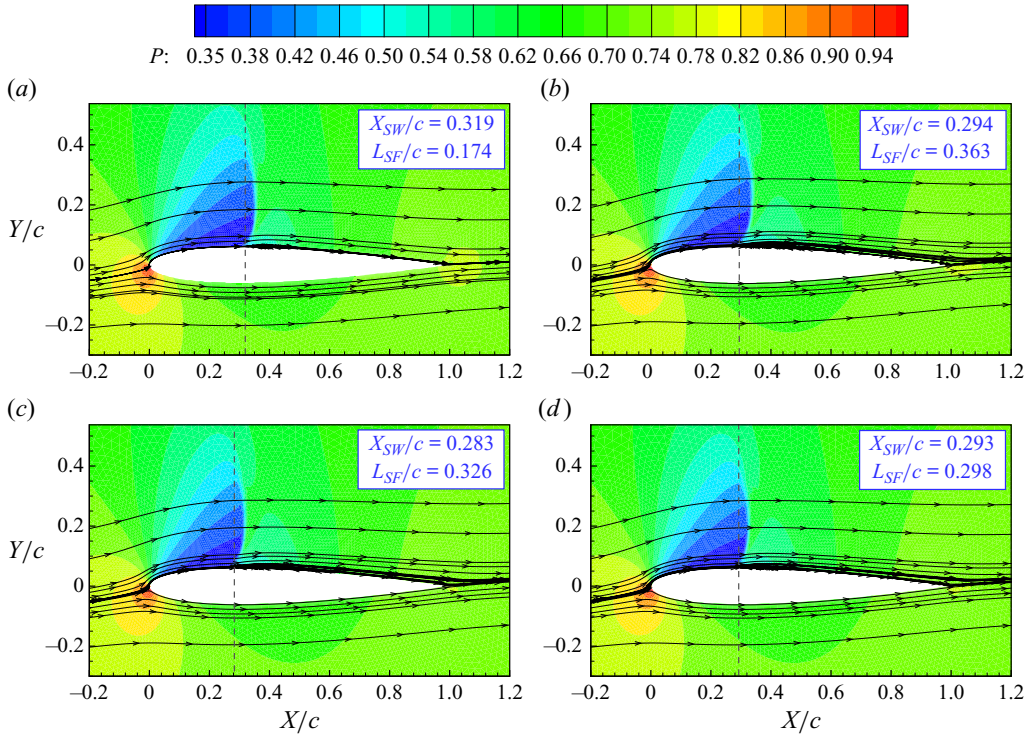
Figure 7. Pressure contours and streamlines in one period at $\alpha = 4.5°$, $Ma = 0.7$ and $Re = 3 \times 10^6$. Here L_{SF} is the length of the flow separation region on the wing surface: (a) $t_1 = 0T$, (b) $t_2 = 1/4T$, (c) $t_3 = 1/2T$, (d) $t_4 = 3/4T$.
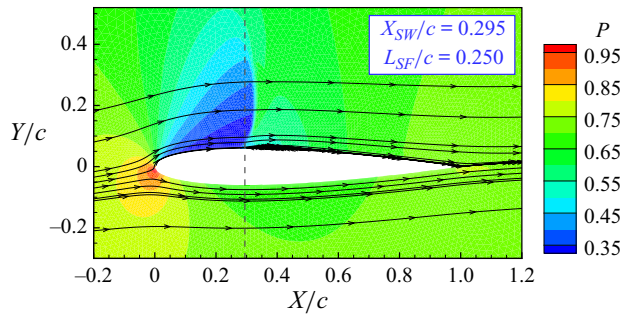

Figure 8. Pressure contours and streamlines of the steady flow field at $\alpha = 4.5°$.

dimensionless pressure (p) contour plots at typical moments are presented in figures 6 and 7, for the unsteady flow field at $\alpha = 5.5°$ and the convergence process at $\alpha = 4.5°$ flow. Vertical dashed lines indicate the position of shock feet. It is evident that in the supersonic buffeting flow, there are significant changes in the oscillation amplitude of shock waves, as well as in the size and position of the flow separation region. During the convergence process in subcritical buffeting flow, shock wave oscillation amplitudes are small, and the left-hand side of the flow separation region remains close to the shock foot, with minor variations on the right-hand side corresponding to shock oscillations. Figure 8 presents the pressure contour plot of the steady flow field at $\alpha = 4.5°$, while figure 9 provides
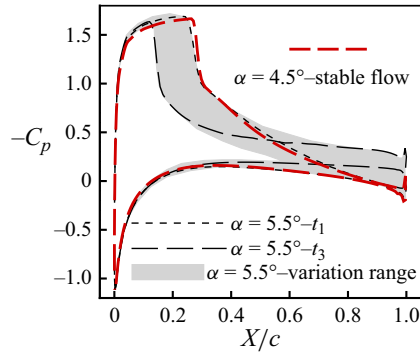
999 A24-10

Figure 9. Pressure coefficient curve of supercritical/subcritical buffet flow field.

the surface pressure coefficient ($C_p = 2(p - p_\infty)/(\rho V^2)$) curve of the steady flow field at $\alpha = 4.5°$, compared with the dynamic pressure coefficient curve of the unsteady flow field at $\alpha = 5.5°$. It can be observed that the shock wave position in the subcritical flutter flow field is further aft, while the oscillation range of the shock wave in the supercritical flutter is entirely ahead of the shock wave position in the subcritical state. Because the impact of the fluid mode on the structural mode is too strong in the supercritical transonic buffeting flow, α is selected as $4.5°$ in the present work.

Below is the structural set-up for the aeroelastic case. For a 2DOF elastic system, with the dimensionless time $\tau = \omega_\alpha \times t$, the above matrices and vectors are evaluated as:

$$
\left.
\begin{aligned}
\boldsymbol{M} &= \begin{bmatrix} 1 & x_\alpha \\ x_\alpha & r_\alpha^2 \end{bmatrix}, \quad
\boldsymbol{K} = \begin{bmatrix} (\omega_h/\omega_\alpha)^2 & 0 \\ 0 & r_\alpha^2 \end{bmatrix} \\[4pt]
\boldsymbol{Q} &= \frac{1}{\pi} V^{*2} \begin{Bmatrix} -(C_l - C_{l0}) \\ 2(C_m - C_{m0}) \end{Bmatrix}, \quad
\boldsymbol{\xi} = \begin{Bmatrix} h/b \\ \theta \end{Bmatrix}.
\end{aligned}
\right\}
\tag{2.3}
$$

In the definition of dimensionless parameters, traditional conventions are followed: aerodynamic parameters such as the Reynolds number and force coefficients are non-dimensionalized using the chord length c (or $2b$), while structural parameters such as the reduced frequency, mass static margin, mass ratio and elastic axis position are non-dimensionalized using the half-chord length b. As shown in (2.3) and figure 3, Ma and $Re = \rho U_\infty c/\mu_f$ represent the Mach and Reynolds number of the free stream, where ρ, U_∞ and μ_f respectively represent the density, the velocity and the viscosity coefficient of the free stream. Parameters C_l and C_m are the coefficients of the lift and pitching moment non-dimensionalized by $C_f = 2F/(\rho U_\infty^2)$, where F represents aerodynamic concentrated force. Parameters C_{l0} and C_{m0} are the mean value of the lift and pitching moment coefficients.

The term h/b represents the airfoil heaving displacement and θ represents the airfoil pitching angle. Frequency $k = \omega b/U_\infty$ is the reduced frequency non-dimensionalized by b, natural frequency ω and U_∞. Therefore, k_h represents the dimensionless natural heaving (plunging) frequency and k_α represents the dimensionless natural pitching frequency. Ratio $\mu = m/(\pi \rho b^2)$ is the non-dimensional mass ratio, where m represents the mass of the wing. Radius r_a is the gyration radius of the airfoil around the elastic axis. Velocity $V^* = U_\infty/(\omega_\alpha b \mu^{1/2}) = 1/(k_\alpha \mu^{1/2})$ is the non-dimensional velocity. Parameter x_a is the

airfoil static unbalance, which represents the dimensionless distance between the centre of gravity and the elastic axis. The position of the elastic axis and x_a are non-dimensionalized by b. Distance a is the dimensionless distance of the elastic axis after the midpoint of the airfoil, which will comprehensively affect the mutual coupling of each fluid/structure mode. The elastic axis is set at $0.224c$ from the leading-edge point, which is the common position in the research of transonic buzz.

2.3. *Unsteady aerodynamic models*

The process of modelling is introduced in Step 1 of figure 2. An identification technique is used to construct the ROM. The time cost of the ROM-based flutter analysis mainly lies in training the model. Because the unsteady loads are computed in a discrete domain, the model is chosen for the two-input–two-output system, as shown in (2.4a,b):

$$\boldsymbol{u} = \begin{bmatrix} h/b \\ \theta \end{bmatrix}, \quad \boldsymbol{y}_f = \begin{bmatrix} C_l - C_{l0} \\ C_m - C_{m0} \end{bmatrix}. \tag{2.4a,b}$$

The ARX model (Zhang *et al.* 2007) is used to build the aerodynamic ROM. The ARX model is based on difference equations, and it can be expressed as follows:

$$\boldsymbol{y}_f(k) = \sum_{i=1}^{na} \boldsymbol{A}_i \boldsymbol{y}_f(k-i) + \sum_{i=0}^{nb-1} \boldsymbol{B}_i \boldsymbol{u}(k-i), \tag{2.5}$$

where $\boldsymbol{y}$ is the system output and $\boldsymbol{u}$ is the input. Orders of the model chosen by the user are *na* and *nb*. The output of the current step is always determined by the linear combination of the previous *na* steps' output and the previous $nb-1$ steps' input. The delay parameters (*na*, *nb*) determine the prediction accuracy of the model in unsteady flow. Coefficients $\boldsymbol{A}_i$ and $\boldsymbol{B}_i$ are constant coefficients to be estimated. The least-squares method is used to estimate unknown model parameters. To achieve a zero mean, the constant levels need to be removed from the data before they are estimated. This is mainly for two reasons. One is to eliminate the influence of static aeroelastic deformation on the system as much as possible in numerical studies. The second is to improve the accuracy of the autoregressive architecture model, where the sample data need to meet the zero-input zero-output characteristic.

In order to obtain the state-space aeroelastic model, we define a state vector $\boldsymbol{x}_f(k)$ consisting of $(na + nb - 1)$ vector states as follows:

$$\boldsymbol{x}_f(k) = [y_f(k-1), \ldots y_f(k-na), u(k-1), \ldots, u(k-nb+1)]^{\mathrm{T}}. \tag{2.6}$$

The state-space form of the discrete-time aerodynamic model is as follows:

$$\left. \begin{aligned} \boldsymbol{x}_f(k+1) &= \boldsymbol{A}_a \boldsymbol{x}_f(k) + \boldsymbol{B}_a \boldsymbol{u}(k) \\ \boldsymbol{y}_f(k) &= \boldsymbol{C}_a \boldsymbol{x}_f(k) + \boldsymbol{D}_a \boldsymbol{u}(k), \end{aligned} \right\} \tag{2.7}$$

where

$$
A_a =
\begin{bmatrix}
A_1 & A_2 & \cdots & A_{na-1} & A_{na} & B_1 & B_2 & \cdots & B_{nb-2} & B_{nb-1} \\
I & 0 & \cdots & 0 & 0 & 0 & 0 & \cdots & 0 & 0 \\
\vdots & I & \cdots & 0 & 0 & 0 & 0 & \cdots & 0 & 0 \\
\vdots & \vdots & \ddots & \vdots & \vdots & \vdots & \vdots & \ddots & \vdots & \vdots \\
0 & 0 & \cdots & I & 0 & 0 & 0 & \cdots & 0 & 0 \\
0 & 0 & \cdots & 0 & 0 & 0 & 0 & \cdots & 0 & 0 \\
0 & 0 & \cdots & 0 & 0 & I & 0 & \cdots & 0 & 0 \\
0 & 0 & \cdots & 0 & 0 & 0 & I & \cdots & 0 & 0 \\
\vdots & \vdots & \ddots & \vdots & \vdots & \vdots & \vdots & \ddots & \vdots & \vdots \\
0 & 0 & \cdots & 0 & 0 & 0 & 0 & \cdots & I & 0
\end{bmatrix},
$$

$$
B_a = [B_0 \ \ 0 \ \ 0 \ \ \cdots \ \ 0 \ \ I \ \ 0 \ \ 0 \ \ \cdots \ \ 0]^{\mathrm{T}},
$$

$$
C_a = \begin{bmatrix} A_1 & A_2 & \cdots & A_{na-1} & A_{na} & B_1 & B_2 & \cdots & B_{nb-2} & B_{nb-1} \end{bmatrix},
$$

$$
D_a = [B_0].
$$

(2.8)

To couple the structural equations, the discrete-time form equation is turned into the continuous-time form, and the model in the state-space form is constructed as follows:

$$
\left.
\begin{aligned}
\dot{x}_f(t) &= A_a x_f(t) + B_a u(t) \\
y_f(t) &= C_a x_f(t) + D_a u(t).
\end{aligned}
\right\}
$$

(2.9)

2.4. *Aeroelastic models*

The structural state vector is defined as $x_s = [\theta, h/b, \dot{\theta}, \dot{h}/b]^{\mathrm{T}}$ for the 2DOF case, and the structural motion equation (2.2) in state-space form can be rewritten as

$$
\left.
\begin{aligned}
\dot{x}_s(t) &= A_s x_s(t) + k_\alpha \cdot B_s y_f(t) \\
u(t) &= C_s x_s(t) + k_\alpha \cdot D_s y_f(t),
\end{aligned}
\right\}
$$

(2.10)

where

$$
A_s = \begin{bmatrix} 0 & I \\ M^{-1} \cdot K & M^{-1} \cdot G \end{bmatrix}, \quad
B_s = \begin{bmatrix} 0 \\ M^{-1} \end{bmatrix}, \quad
C_s = [I \ \ 0], \quad
D_s = [0].
$$

(2.11a–d)

Coupling the structural state equation (2.10) with the aerodynamic state equation (2.9), we can get the state equation and output equation of the aeroelastic system as follows:

$$
\begin{Bmatrix} \dot{x}_s(t) \\ \dot{x}_f(t) \end{Bmatrix} =
\begin{bmatrix} A_s + k_\alpha \cdot B_s D_a & k_\alpha \cdot B_s C_a \\ B_a C_a & A_a \end{bmatrix}
\begin{Bmatrix} x_s(t) \\ x_f(t) \end{Bmatrix}.
$$

(2.12)

The analysis of the flutter characteristics is then used to solve the complex eigenvalues in (2.12). The process of the transonic 2DOF flutter analysis is as follows.

(1) Use URANS methodology flow solver to compute the mode aerodynamic coefficients based on the designed input signals.

(2) Use the identification technique to construct the input–output difference model (2.7) in the discrete-time domain, and then turn it into the continuous-time state-space form (2.9).

(3) Couple the aerodynamic state-space equations (2.9) with the structural state-space equations (2.10), to obtain the aeroelastic state-space equation (2.12).

(4) Solve the eigenvalues of the state matrix in (2.12) at different mass ratios and ratios of structural natural frequencies ($i_n = k_h/k_\alpha$); the stability of the aeroelastic system can be analysed by the root loci method. The real and imaginary parts of the eigenvalues are the growth rate and frequency of the aeroelastic system. The damping is usually defined as the opposite of the growth rate. When the growth rate is greater than zero, the system is unstable. On the contrary, the system is stable.

It is noteworthy that the aeroelastic model constructed in this paper is based on a linear model under small disturbances, possessing both time-domain and frequency-domain solving capabilities. The aeroelastic model can accurately and rapidly predict the instability boundary and type of the aeroelastic system, but it cannot precisely predict the nonlinear response of the aeroelastic system.

3. The aerodynamic model and the fluid mode in pre-buffet flow

3.1. *Construction and validation of the aerodynamic model*

Training signal design is the key to dynamics modelling. The training signal should cover the frequencies of the structural modes that need to be excited. The training amplitude should not be too large; otherwise, the aerodynamic responses will be nonlinear, and the linear modelling method cannot be used. Based on similar considerations, random signals that more easily excite flow nonlinearity are not suitable for linear modelling; generally, sweep signals are used. At that pre-buffet state, the flow field still has some potential unsteady features, which may be excited by some very small disturbances. Therefore, we take the steady-state flow field as the initial solution in the training process. The time step of the training signal needs to be moderate: too small a time step can lead to excessively high model dimensions, while too large a step can cause the model to lose high-frequency flow features, potentially resulting in modelling failure. Based on past research experience, it is generally recommended that the entire cycle corresponding to the highest frequency in the training signal should ideally contain 25–30 time steps. In this paper, a chirp signal and its power spectrum density (PSD) are designed as depicted in figure 10. The reduced frequency of the signal is in a broad band of [0.04, 0.80]. Use of CFD yields the aerodynamic response as the output.

The relative errors (3.1) of model training are shown in figure 11:

$$\text{Relative error} = \sum_{t=0}^{t_n} \frac{|\boldsymbol{y}_t - \boldsymbol{y}_{t,pre}|}{|\boldsymbol{y}_t - \overline{\boldsymbol{y}_t}|}. \tag{3.1}$$

The error is up to 10 % when $na = nb = 10$, while for $na = nb = 30$ the error can be reduced to 2.05 %, which satisfies the requirement of accuracy in the subsequent analysis. Therefore, in the present study, the orders of the ROM are $na = nb = 30$, which are larger than those in subsonic or supersonic potential flow. The training results of the ROM are depicted in figure 12.

The model is then validated by comparing the time history of the lift and moment coefficient response between the ROM and CFD. The test signal is depicted in figure 13.
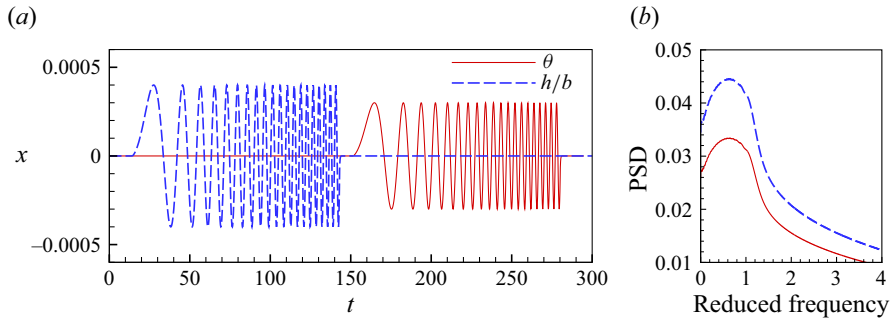
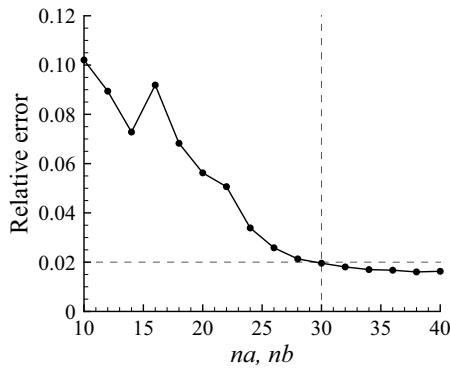Figure 10. (*a*) The training signal with (*b*) its PSD.

Figure 11. Identified errors with different (*na*, *nb*) orders.
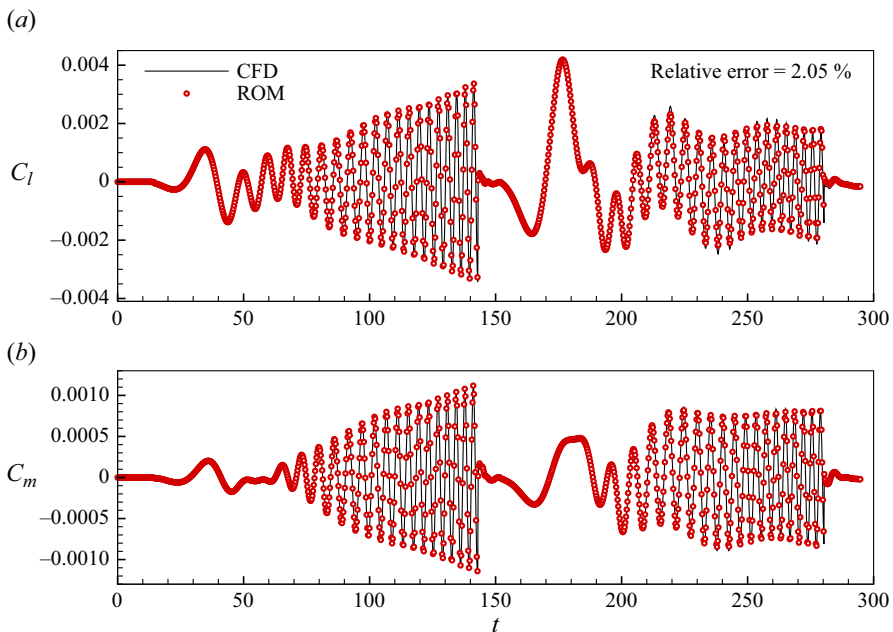

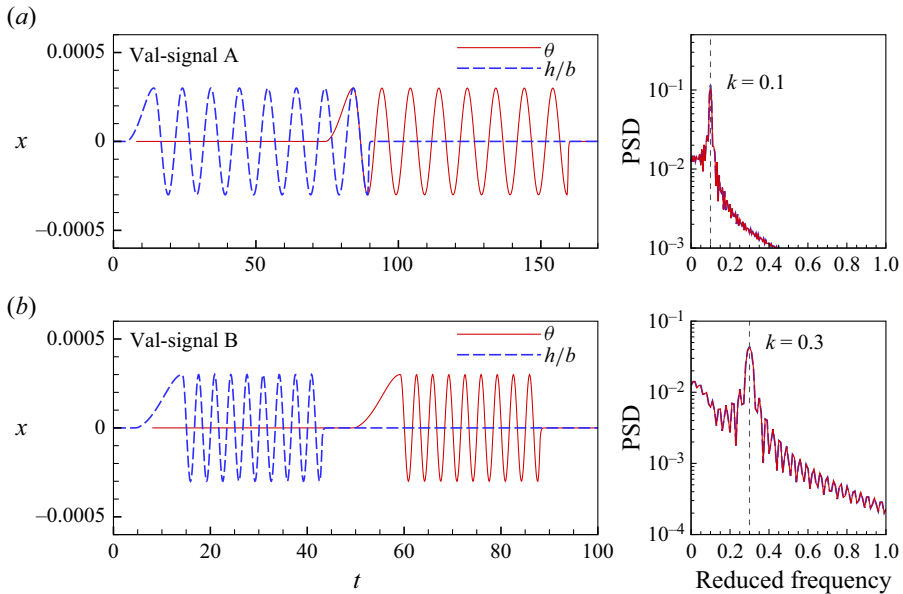Figure 12. The training results of the ROM.

Figure 13. The validation signals. (*a*) Signal A at $k = 0.1$. (*b*) Signal B at $k = 0.3$.
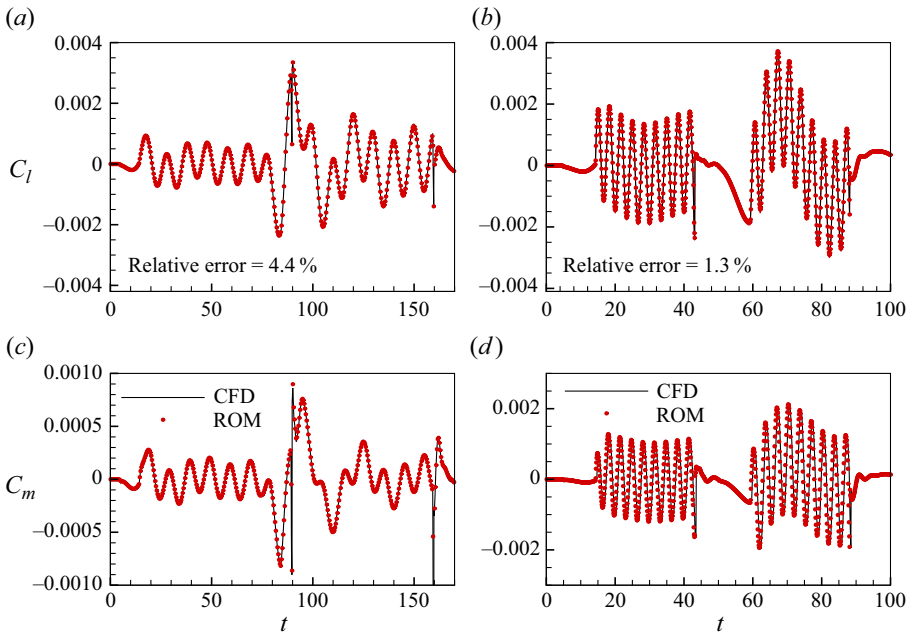

Figure 14. Comparison of the time history of the aerodynamics responses. (*a,c*) The response caused by the excitation of signal A. (*b,d*) The response caused by the excitation of signal B.

The major non-dimensional frequency of signal A is 0.1 and that of signal B is 0.3. Figure 14 presents the time history of the lift and moment coefficient predicted by the ROM, which is in good agreement with that computed by CFD, further verifying the ROM in the present study.
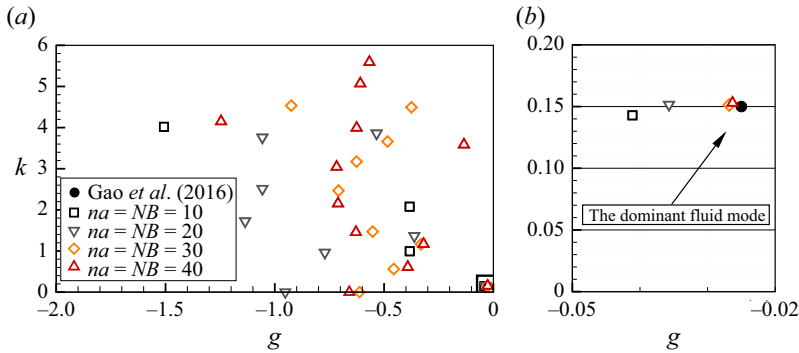
999 A24-16

Figure 15. Eigenvalues of the aerodynamic models for the 2DOF airfoil at various orders; $Ma = 0.7, Re = 3 \times 10^6, \alpha = 4.5°$ (Gao *et al.* 2016*a*).

3.2. *Identification of the fluid mode*

The fluid eigenmode represents the stability of the fluid itself. It significantly affects the coupled-mode flutter and plays a vital role in the SDOF flutter of a spring-mounted airfoil. Therefore, it is necessary to identify and characterize the fluid eigenmode.

The free-stream state is $Ma = 0.7$, $Re = 3 \times 10^6$, $\alpha = 4.5°$, $a = 0.224c$, which is identical to the case presented in § 3.1. Figure 15 shows the distribution of the eigenvalues of the A_a matrix of the model built before. The real part of the complex eigenvalue indicates the growth rate (g) of the fluid eigenmode, while the imaginary part indicates the reduced frequency (k). Matrix A_a is a redundant matrix, and the larger the orders are, the greater is the redundancy of the matrix. Some of the eigenvalues may not represent the real fluid mode. Therefore, the higher damped eigenvalues have a larger scatter with changing orders. However, it can be seen that an eigenvalue almost stays at the point of $(-0.026, 0.155)$ with order increasing. This is closely similar to the fluid mode observed in the previous transonic aerodynamic modelling of an SDOF airfoil, as indicated by the black filled circles in figure 15 (Gao *et al.* 2016*a*). It is also noted that this eigenvalue is the one closest to the imaginary axis, indicating the least stable eigenmode, which implies that its stability margin is the lowest. In the present study, we define this corresponding mode as 'dominant fluid mode' (Gao *et al.* 2016*a*), also called 'least stable mode' (Sartor *et al.* 2015) or 'unstable global mode' (Crouch *et al.* 2009), which is associated with the flow damping and frequency. The fluid mode mentioned later refers to the dominant fluid mode identified here.

This mode and its eigenvalue in the subcritical state can be explicitly displayed by the linear ROM. However, it is difficult to extract this mode in numerical simulations and wind tunnel experiments, because this is a steady state. Here, modal decomposition has been performed by the DMD method for a subcritical buffet flow in the converging process, corresponding to the red dashed line in figure 5. The first four dominant global modes characterized by the pressure contours are shown in figure 16, and the growth rates and reduced frequencies are summarized in table 1. All modes are conjugate modes except the first one; thus a total of seven modes are selected. It can be noticed that both the growth rate and the frequency are zero for the first mode. It is a static mode, close to the mean flow field. All the other modes reflect the oscillating features resulting from shock waves. From table 1, the growth rates of these modes are negative because the snapshots are recorded from the converging process. We also note that the reduced frequency of Mode 2 is 0.162, which is equal to the buffet frequency from the CFD simulation, as shown
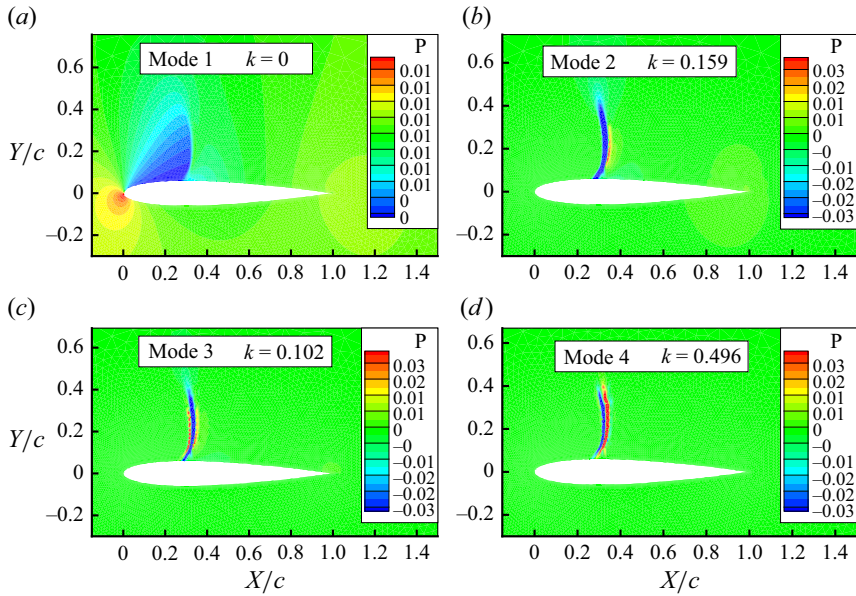
Figure 16. First four dominant global modes from the DMD method of a subcritical buffet flow in the converging process: (*a*) Mode 1, (*b*) Mode 2, (*c*) Mode 3 and (*d*) Mode 4.

Mode	Growth rate	Reduced frequency
1	0	0
2	−0.045	0.162
3	−0.318	0.102
4	−0.503	0.496

Table 1. Growth rates and reduced frequencies of first four dominant DMD modes.

in figure 5. And both of these are close to the frequency of the dominant fluid mode obtained from the unsteady aerodynamic ROM. The growth rate of Mode 2 is −0.045, which differs from the −0.025 obtained using the unsteady aerodynamic ROM. The root of the discrepancy lies in the different flow conditions: the DMD modes are based on a stationary airfoil in the converging process, whereas the unsteady aerodynamic ROM uses aerodynamic responses under structural perturbations. The presence of structural perturbations reduces the stability margin of the pre-buffet flow, consistent with the current findings. The absolute values of the growth rates of Mode 3 and Mode 4 are higher than that of Mode 2. Therefore, Mode 2 is the most important coherent global mode for the present pre-buffet flow, which should be focused on to address the most relevant changes in the flow field and physical mechanisms.

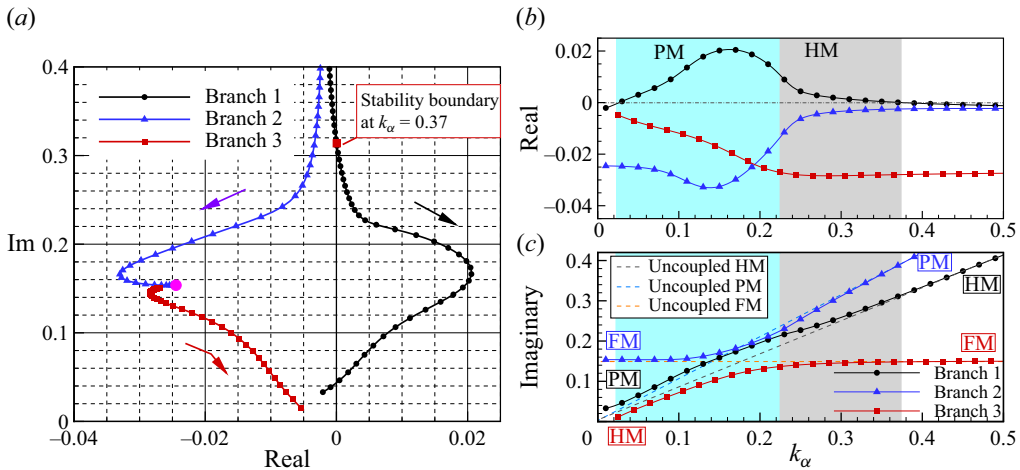Further validation of the linear model and fluid modes in this paper is presented in Appendix C.

999 A24-18

Figure 17. Eigenvalue loci of the aeroelastic system at $k_h/k_\alpha = 0.85$. (*a*) The root loci. (*b*) Real parts and (*c*) imaginary parts of the root loci change with the natural pitching frequency.

4. Dynamic characteristic of aeroelastic problems affected by fluid mode

4.1. *Dynamic characteristics under typical frequency ratio*

This section is dedicated to studying the stability of the aeroelastic system of 2DOF airfoil in the transonic pre-buffet flow and the influences of the related structural parameters, under typical frequency ratios. The aeroelastic model has been established in the state-space form. Solving the eigenvalues of the state matrix in (2.12) at different structural parameters, the stability of the aeroelastic system can be analysed by the root loci method.

The free-stream state and the aerodynamic model have been introduced in § 3.2. For the structural parameters $\mu = 200$, $r_a^2 = 1.036$, $x_a = 0.2$, $k_h/k_\alpha = 0.85$, the eigenvalue loci as the structural natural pitching frequency k_α decreases are depicted in figure 17(*a*). The horizontal (vertical) axes represent the real (imaginary) parts of the eigenvalue. The real parts mean the growth rate of the coupled aeroelastic system and the imaginary parts represent the frequency. In our aeroelastic model, negative growth rate (positive damping) represents that the system is stable, while positive growth rate (negative damping) indicates that the system is unstable. It can be found that there are a total of three branches, which we label herein as Branch 1 (the black circle line), Branch 2 (the blue triangle line) and Branch 3 (the red square line). The purple point represents the least stable fluid mode and the arrow points in the direction of decreasing natural frequency. The eigenvalues of Branch 1 march towards the imaginary axis and further cross into the right half-plane, resulting in instability (flutter) of the coupled system. The flutter boundary predicted by the aeroelastic model is at $k_\alpha = 0.37$.

Figure 18 shows a comparison of the time history of the heaving displacement and the pitching angle between the coupled CFD and CSD methods and the aeroelastic model simulation in the vicinity of the flutter boundaries at $k_h/k_\alpha = 0.85$. The results computed by the aeroelastic model agree well with those obtained by the coupled CFD and CSD methods, further verifying the aeroelastic model in the present study. The flutter boundary at various frequency ratios has also been confirmed through the CFD–CSD method, as denoted in figure 27 of § 5 with red open squares.
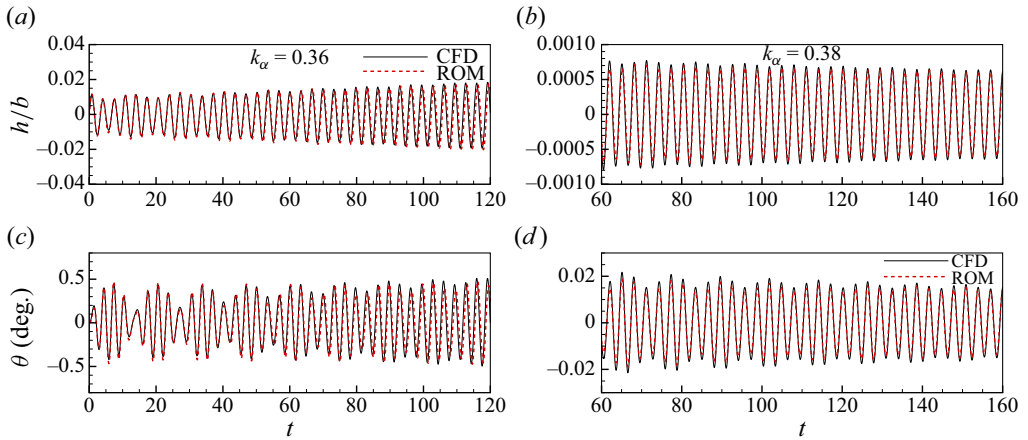
Figure 18. Comparison of the time history of the heaving displacement and the pitching angle between the coupled CFD–CSD method and the aeroelastic model, $Ma = 0.7$, $Re = 3 \times 10^6$, $\alpha = 4.5°$, $k_h/k_\alpha = 0.85$, $\mu = 200$, for (*a,c*) $k_\alpha = 0.36$ and (*b,d*) $k_\alpha = 0.38$.

The aeroelastic system consists of three main modes: fluid mode, heaving mode and pitching mode. However, the relationship between branches of the eigenvalue loci and coupled modes of the aeroelastic system cannot be directly reflected in figure 17(*a*). It is necessary to determine which modes these three branches represent at each value of the natural frequency. Indeed, the hidden coupled pitching mode can be represented by Branch 1 at one value of the natural frequency and switch to Branch 2 or Branch 3 at another value of the natural frequency (or vice versa). This process is described as mode veering by Gao *et al.* (2017*b*).

For further analysis, the real and imaginary parts of the eigenvalue varying with the natural pitching frequency are displayed in figures 17(*b*) and 17(*c*), respectively. The grey and blue colour blocks respectively represent the region of heaving instability and that of pitching instability. Since the coupled modes switch between branches with the change of the natural frequency, the left and right sides of branches in figure 17(*c*) are marked with the coupled mode types: coupled fluid mode (FM), coupled heaving mode (HM), coupled pitching mode (PM). The grey, blue and orange dashed lines are used to mark the uncoupled heaving, pitching and fluid modes.

The type of the coupled mode represented by a branch can be determined by the imaginary parts of the branch. The frequency of the fluid mode is almost constant, and the heaving and pitching modes have a fixed frequency ratio. Based on this, the types of coupled modes are distinguished. Certainly, in fluid–structure coupled aeroelastic systems, the modes reflected by the system's eigenvalue are all coupled. The purpose of resolving these modes through the aforementioned method is to better understand the coupled system through a linear aeroelastic model.

The coupled modes represented by the three branches undergo complex mode veering processes. As the natural pitching frequency k_α decreases (the non-dimensional velocity V^* increases), Branch 1 veers from HM to PM; Branch 2 veers from PM to FM; and Branch 3 veers from FM to HM. The mode veering occurs within the instability region $(0.02, 0.37)$ of Branch 1, so there are two kinds of flutter before and after the mode veering. As shown in figure 12, the mode veering phenomenon is actually a continuous process with $k_\alpha = (0.14, 0.22)$, rather than a sharp transition. Within this transition range, it is
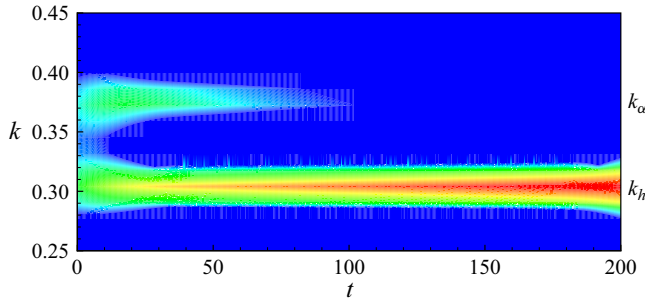
999 A24-20

Figure 19. Wavelet transform diagrams for the responses of pitching mode calculated by CFD–CSD at $k_h/k_\alpha = 0.85$ and $k_\alpha = 0.36$.

difficult to determine the correspondence between the branches and the coupled modes. For simplification, we define the boundary at $k_\alpha = 0.22$, where the response frequency of Branch 1 is in the middle of the natural frequencies of the structural heaving and pitching modes. Consequently, the instability range of Branch 1 is qualitatively divided into the PM and HM ranges.

The grey block represents the SDOF heaving flutter region at $k_\alpha = (0.22, 0.37)$. In the initial stage of the region (right-hand side), the coupled frequencies of the heaving and pitching modes do not shift relative to their natural frequencies. So it should be defined as the SDOF heaving flutter. This region is far from the instability boundary of the SDOF heaving airfoil ($k_h < 0.14$). On the contrary, it is within the instability boundary of the SDOF pitching airfoil ($0.13 < k_\alpha < 0.42$). This special phenomenon is caused by the coupling of the fluid mode, heaving mode and pitching mode. Therefore, if the pitching mode is decoupled from the 2DOF aeroelastic system, the SDOF heaving flutter phenomenon will no longer exist in this region, although the pitching mode does not obviously participate in the coupling.

Figure 18 also corroborates our judgment on SDOF heaving flutter. We present the wavelet transform diagrams of the time-domain responses calculated by CFD–CSD in figure 18(c), as shown in figure 19. It can be seen that, due to the initial disturbances applied to both the heaving and pitching modes, their responses initially vibrate in their natural modes. Over time, the natural modes transition to the coupled modes. It can be observed that the natural pitching mode gradually disappears and transitions to the coupled mode, which is almost identical to the natural heaving mode.

The blue block at $k_\alpha = (0.02, 0.22)$ represents the coupled-mode flutter, in which the pitching mode is unstable. This is based on the fact that Branch 1 represents the coupled pitching mode after the mode veering. At the beginning of this region, the frequency of the coupled pitching mode is between the uncoupled natural pitching frequency and the natural heaving frequency. The structural natural frequency is low, which is different from the instability boundary of the SDOF pitching airfoil.

4.2. *The effect of structural parameters*

Regarding the previous paragraph on the determination of two distinct vibration types, further analysis and explanation are required. We analyse the influences of two structural parameters (x_a, μ) on the aeroelastic system. Firstly, the effect of x_a changes on the aeroelastic system is investigated. Parameter x_a is the airfoil static unbalance (dimensionless distance between the centre of gravity and the elastic axis), which is an
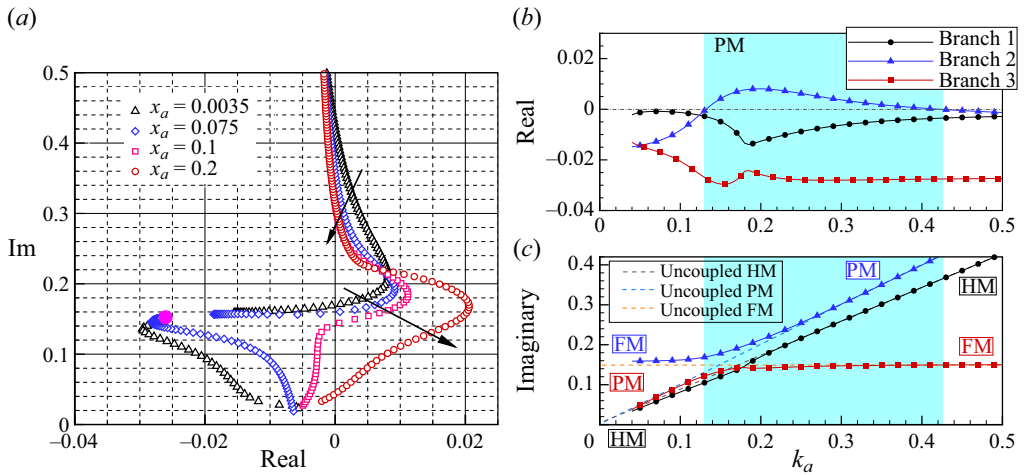
Figure 20. (*a*) The unstable branch of the eigenvalue loci at $k_h/k_\alpha = 0.85$ with different x_a. (*b*) Real parts and (*c*) imaginary parts of the root loci change with the natural pitching frequency at $k_h/k_\alpha = 0.85$ and $x_a = 0.0035$.

important parameter that affects the coupling of heaving and pitching modes. When x_a is close to zero or negative, the critical dimensionless wind speed of the coupled-mode flutter is large. Conversely, when x_a increases, the critical wind speed of the flutter will decrease. The value of x_a is set as 0.0035 in the BACT model. In our simulations, the airfoil is fixed at $0.224c$ from the leading edge ($a = -0.554b$) in both the CFD–CSD simulation and the aeroelastic model. The change in x_a actually reflects a change in the centre of gravity position, meaning that it only requires modifying the structural model rather than the unsteady aerodynamic model. Therefore, this study can conveniently investigate the impact of changes in x_a on the aeroelastic system.

A typical frequency ratio of 0.85 is selected, with $x_a = (0.0035, 0.075, 0.1, 0.2)$. For convenience of understanding, only the unstable branches of the eigenvalue are presented in figure 20(*a*). It can be observed that as x_a increases, the upper boundary of the instability region decreases, while the lower boundary rapidly increases. Around $x_a = 0.1$, the coupling form of the aeroelastic system changes, and the instability region at low frequency increases from scratch. To further investigate this phenomenon, the root locus of the aeroelastic system at $x_a = 0.0035$ and $k_h/k_\alpha = 0.85$ has been added, as shown in figure 20(*b*,*c*). Branch 1 always represents the structural heaving mode. There is a transition between Branch 2 and Branch 3, where the fluid mode veers to the pitching mode. Only Branch 2 has an unstable region. At the right-hand boundary of the instability region, the response frequency is locked to the natural pitching frequency. At the left-hand boundary, the response frequency is equal to the flow frequency. Therefore, it should be defined as an SDOF pitching flutter induced by the fluid mode. This is a completely different coupling form from that of the aeroelastic system at $x_a = 0.2$, as shown in figure 17(*b*,*c*). The coupled-mode flutter and SDOF heaving flutter that occurred at $x_a = 0.2$ no longer manifest at $x_a = 0.0035$. In summary, changes in x_a can alter the region of instability, the mode of instability and the form of coupling. Increasing x_a will enhance the coupling between structural modes and suppress the SDOF flutter.

The following explores the influences of mass ratio on the aeroelastic system. Similarly, a frequency ratio of 0.85 and a kind of mass ratio (50, 100, 200, 400, 800) are selected, as
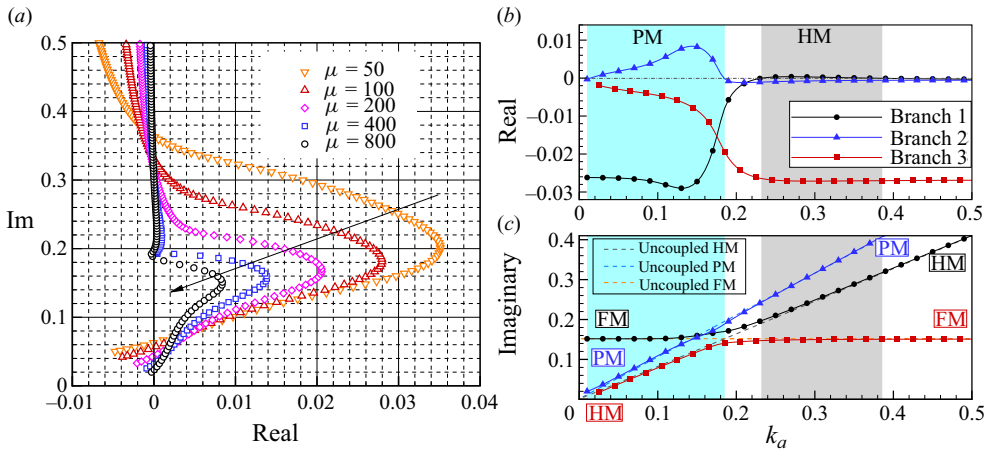
999 A24-22

Figure 21. (*a*) The unstable branch of the eigenvalue loci at $k_h/k_\alpha = 0.85$ with different μ. (*b*) Real parts and (*c*) imaginary parts of the root loci change with the natural pitching frequency at $k_h/k_\alpha = 0.85$ and $\mu = 800$.

depicted in figure 21(*a*). It can be observed that as the mass ratio increases, the upper boundary of the instability interval decreases and the lower boundary also decreases. Around a mass ratio of 400, the system undergoes some changes. When the response frequency is around 0.2, the system returns to a stable state. To further investigate this phenomenon, the root locus of the aeroelastic system at $\mu = 800$ and $k_h/k_\alpha = 0.85$ has been added, as shown in figure 21(*b,c*). Branch 2 only represents the pitching mode and the fluid mode veers to the heaving mode. It can be clearly seen here that the instabilities of coupled pitching and heaving modes are separate, supporting the aforementioned judgment. Thus, the conclusion is that increasing the mass ratio can eliminate the mode veering phenomenon as much as possible without changing the vibration properties of the system.

4.3. *Various aeroelastic phenomena under different natural frequencies*

In § 4.1, we analysed the flutter characteristics and types of the aeroelastic systems for frequency ratios of 0.85, as k_α varies. However, one frequency ratio is merely demonstrated in one line within the two-dimensional parameter space composed of k_h and k_α. In order to establish a more comprehensive understanding of the flutter mechanism, this section analyses the flutter characteristics within the two-dimensional parameter space (k_h, k_α) at $\mu = 200$ and $x_a = 0.2$. Based on the analysis method in § 4.2, multiple distinct frequency ratios were analysed within $i_n = k_h/k_\alpha = (0.2, 5)$. Then, the flutter characteristics were obtained by connecting the boundaries of various aeroelastic phenomena under different frequency ratios, as depicted in figure 22.

There are six distinct aeroelastic phenomena: SDOF heaving flutter, SDOF pitching flutter, heaving instability within coupled-mode flutter, pitching instability within coupled-mode flutter, forced vibration and stable state. The horizontal (vertical) axes represent the natural dimensionless frequencies of airfoil pitching (heaving) mode. The colour blocks and numbers in the two-dimensional graphs represent the type of vibration. Multiple vibration types are converted near the 45° symmetry dashed line. The wide variety of distinct aeroelastic phenomena is the result of the joint coupling of the fluid mode, structural heaving mode and structural pitching mode.
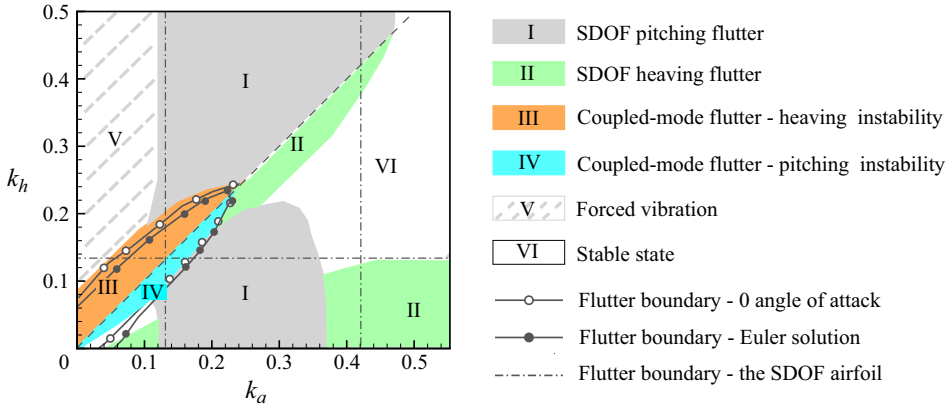
Figure 22. Various aeroelastic phenomena within the two-dimensional parameter space (k_h, k_α).

The following provides a detailed introduction to each of the six types. It is noteworthy that the stability boundaries predicted by the aeroelastic model are quite accurate, as demonstrated in figure 18 and the open red squares in figure 27. However, the boundaries between different aeroelastic phenomena are determined empirically. In fact, the transition is continuous rather than discrete. Therefore, these internal boundaries are merely schematic representations.

I – SDOF pitching flutter. Two grey areas. For the upper area, due to the high frequency of the heaving mode, the instability boundary is highly similar to that of the SDOF pitching airfoil. For the lower area, there are many complex phenomena due to the participation of the heaving mode. Coupled-mode flutter on the left-hand side (region III/IV) and SDOF heaving flutter on the right-hand side (region II) have encroached upon the region of SDOF pitching flutter.

II – SDOF heaving flutter. The lower areas of region II fall within the instability boundary of the SDOF heaving airfoil and are separated by region I. This occurs because the positive growth rate of SDOF pitching flutter is much greater than that of SDOF heaving flutter. Additionally, the remaining area lies below the 45° line, where the natural heaving frequency exceeds the instability boundary of the SDOF heaving airfoil.

III/IV – coupled-mode flutter. The distribution is symmetrical around the 45° line within the range of low natural frequencies, with the upper part representing the instability of the heaving mode and the lower part representing the instability of the pitching mode. Upon comparing the black solid line with the open/filled circles, minimal differences can be observed in the boundaries of coupled-mode flutter. Additionally, numerous other complex phenomena depicted in figure 22 primarily originate from the fluid mode.

V – forced vibration. The areas with grey stripes. Existing research has found that elastic structures can cause a reduction in the transonic buffeting boundary $(Ma = 0.7, \alpha = 3.9°)$ (Gao, Zhang & Ye 2018). This phenomenon is also observed in this study. In the area where the structural modes are stable and the natural frequency is low, forced vibration caused by buffeting flow occurs. Detailed analysis of this phenomenon is presented in § 5.3.

VI – stable state. In the top right corner, all fluid/structure modes of the aeroelastic system remain stable due to the high structural frequency. In the lower left corner, all modes are stabilized as a result of the complex coupling and interference between these modes.
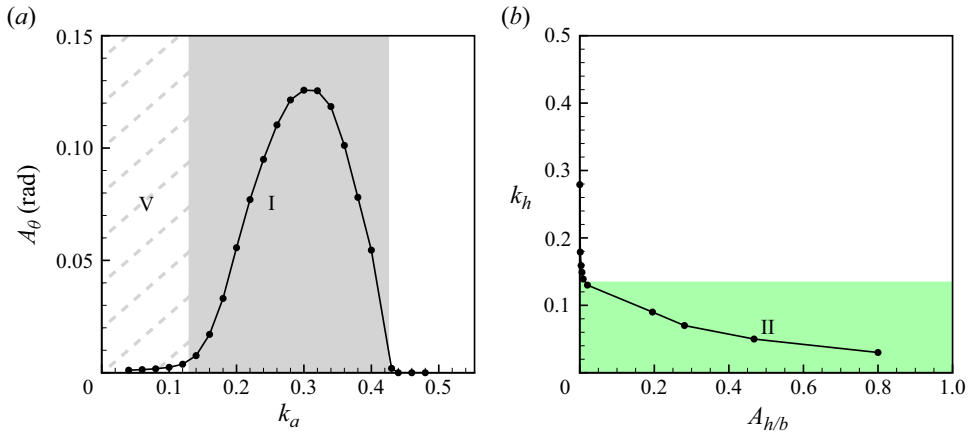
Figure 23. The stability boundaries and the LCO amplitudes of SDOF aeroelastic system of NACA0012 airfoil. (*a*) The SDOF pitching aeroelastic system and (*b*) the SDOF heaving aeroelastic system.

These complex aeroelastic phenomena can be analysed from two perspectives using auxiliary lines. The first perspective is the effect of the fluid mode on a 2DOF aeroelastic system, which is discussed in detail in § 4.4. The second perspective is the effect of the coupling with another structural mode on the SDOF flutter (transonic buzz). In figure 22, the vertical dash-dot lines represent the flutter boundaries ($k_\alpha = (0.13, 0.42)$) of the SDOF pitching airfoil case depicted in figure 23(*a*), while the horizontal dash-dot line represents the flutter boundaries ($k_h = (0, 0.138)$) of the SDOF heaving airfoil case depicted in figure 23(*b*). The black dashed lines represent the LCO amplitudes computed using the CFD–CSD method at different natural frequencies. By comparing the results of figure 22 with the two cases mentioned above, the influence of the coupling of other structural modes on SDOF flutter can be observed. There are two distinct phenomena. The first is that the SDOF heaving flutter occurs at a high natural frequency ($i_n = (0.8, 1)$, $k_h = (0.2, 0.4)$), which is discussed in §§ 4.1 and 4.2. The second is that the SDOF flutter disappears by coupling with another structural mode, at $i_n = (0.3, 0.8)$, $k_\alpha = (0.3, 0.42)$ and $i_n = (0.3, 0.5)$, $k_\alpha = (0, 0.12)$. A detailed study and mechanistic analysis of this phenomenon are presented in § 5.2.

4.4. *The effect of the fluid mode on the flutter boundary*

In figure 22, the black line with open circles represents the coupled-mode flutter boundary of the airfoil under the same parameters at $\alpha = 0°$. While the black line with filled circles represents the flutter boundary of the airfoil under Euler solution at $\alpha = 4.5°$. Our goal is to eliminate the dominant fluid mode in the above two ways. The first approach involves staying away from the buffeting boundary as much as possible, and the second approach is to eliminate the fluid viscosity. The basis for these two approaches is the paper of Karnick & Venkatraman (2017), which found that the viscous effects manipulate the flow by influencing the strength and location of the shock such that the flutter boundary changes significantly. The eigenvalues of the A_a matrix for both cases are depicted in figure 24. The most dominant eigenvalue becomes the zero-frequency mode near the point of $(-0.12, 0)$. Notably, the dominant fluid mode at the point of $(-0.026, 0.155)$ in the case under NS solution at $\alpha = 4.5°$ has been successfully eliminated using both approaches.
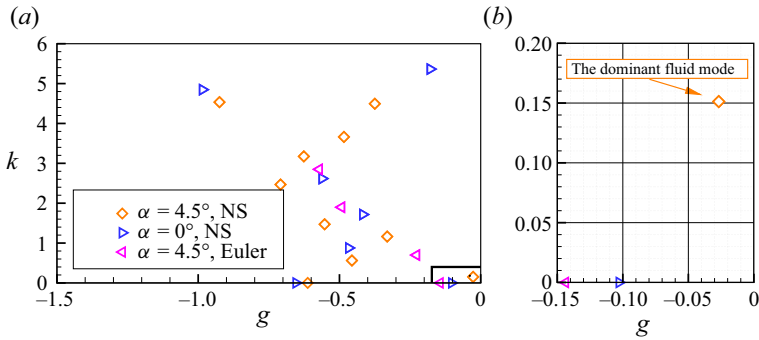
Figure 24. Eigenvalues of the aerodynamic models under different conditions.

A more detailed discussion on the variation of fluid modes with the AOA is presented in Appendix C.

By comparing the three cases mentioned above, we can qualitatively analyse the influence of the fluid mode on the aeroelastic system. The flutter boundaries of these cases are shown in figure 25. Case A corresponds to $\alpha = 4.5°$ under NS solution, Case B represents $\alpha = 0°$ under NS solution and Case C is at $\alpha = 4.5°$ under Euler solution. The lower horizontal axis displays the arctangent of k_h/k_α, while the upper horizontal axis represents $k_h/k_\alpha = i_n$ directly. The vertical axis indicates the non-dimensional flutter velocity ($V_f^* = 1/(k_{\alpha f}\mu^{1/2})$). The flutter boundaries of Case B and Case C are similar and exhibit an approximately axisymmetric distribution. Their flutter velocities decrease as k_h/k_α approaches one and increase as it deviates from one. When $k_h/k_\alpha < 1$, Case B has lower flutter velocities compared to Case C, while the opposite holds true when $k_h/k_\alpha > 1$. Notably, the flutter velocity of Case A is significantly smaller than that of Case B and Case C. Figure 26 shows the root loci for these three cases at $k_h/k_\alpha = 0.85$, corresponding to the blue dashed line in figure 25. Case A has been thoroughly discussed in §§ 4.1 and 4.2. The flutter boundary is located at $V_f^* = 0.19$, and the flutter type is SDOF flutter. For Case B and Case C, there is no mode veering between branches after the dominant fluid mode disappears. Branch 1 represents the coupled heaving mode, while Branch 2 represents the coupled pitching mode, as shown in figures 26(c)–26(f). Unlike Case A, under the critical state of flutter, the frequencies of the coupled modes of Case B and Case C approach each other, representing a coupled-mode flutter. The non-dimensional flutter velocities of Case B and Case C are 0.35 and 0.38, respectively, which are higher than that of Case A. The presence of the fluid mode transforms the type of flutter from coupled-mode flutter to SDOF flutter at the boundary, significantly reducing the flutter boundary. This finding is consistent with the experimental observations conducted by NASA (Rivera *et al.* 1992; Dansberry *et al.* 1993), where an increase in *Ma*/AOA leads to a decrease in transonic flutter velocity, with the response frequency locked to the uncoupled structural frequency (vacuo natural frequency). These experimental results align with the findings and perspectives presented in this study, mutually reinforcing their validity.

5. Mechanism analysis and validation

As mentioned in § 2.4, the aeroelastic model presented in this paper is a linear model and cannot predict the nonlinear aeroelastic responses of coupled systems with high accuracy. However, we believe that the types of aeroelastic problems in this case are dominated by linear characteristics. To further validate the six aeroelastic phenomena predicted by the
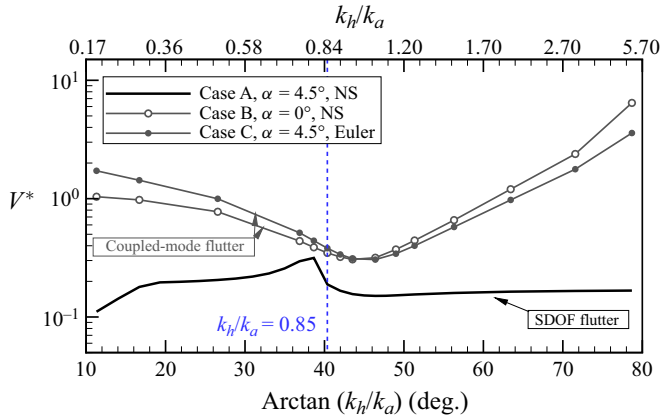
Figure 25. The flutter boundaries varying with k_h/k_α under different conditions.
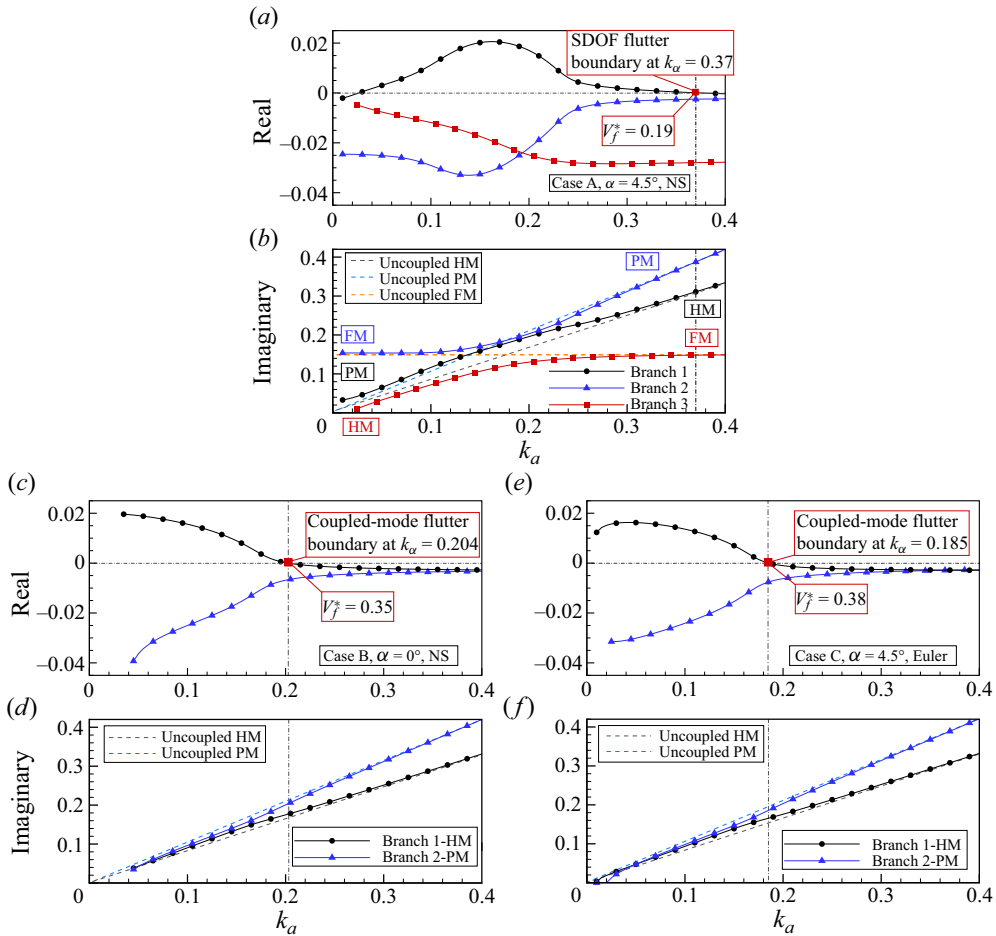

Figure 26. Real part and imaginary part of the root loci change with the natural pitching frequency at $k_h/k_\alpha = 0.85$: (a,b) $Ma = 0.7, \alpha = 4.5°$ under NS solution; (c,d) $Ma = 0.7, \alpha = 0°$ under NS solution; (e,f) $Ma = 0.7, \alpha = 4.5°$ under Euler solution.
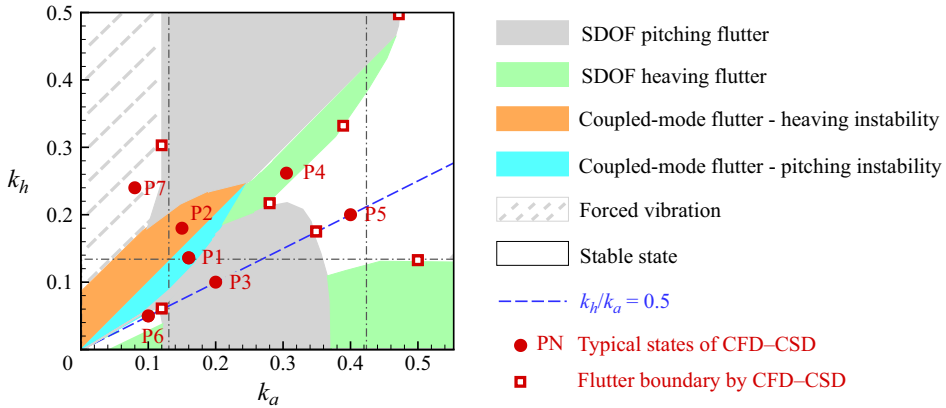
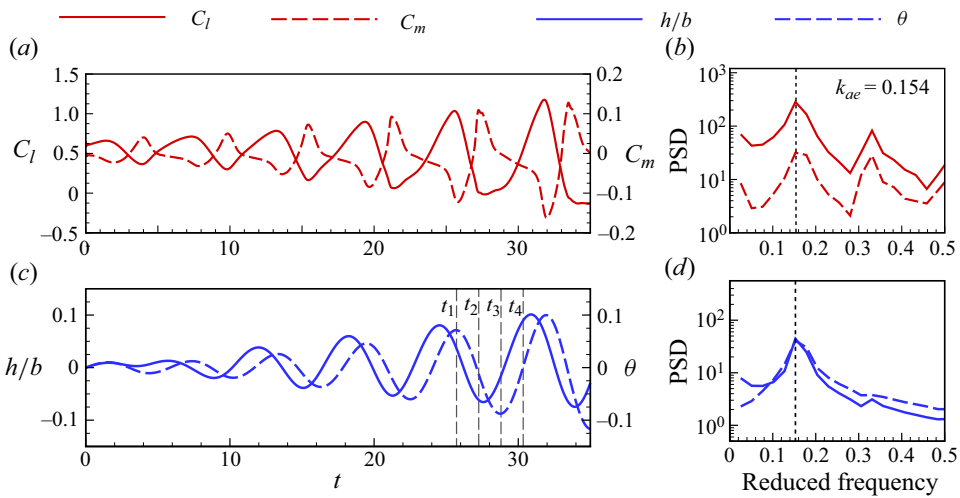Figure 27. The root loci and the time-domain responses of typical states.

Figure 28. Pitching instability of coupled-mode flutter at P1: $k_h = 0.136$, $k_\alpha = 0.16$. (*a*) Force coefficients, (*c*) displacements, (*b,d*) PSD, $k_{ae} = 0.15 = 0.94k_\alpha$.

aeroelastic model, the CFD–CSD method was conducted to verify for the states denoted as the red circles with labels P1 to P7 in figure 27. The red open squares indicate the flutter boundary calculated by the CFD–CSD method. The blue dashed line represents the root loci of the frequency ratio of 0.5. In figures 28 to 43, k_{ae} represents the dominant frequency of the response and k_b represents the buffeting frequency. The red solid (dotted) line represents the lift (moment) coefficient and the blue solid (dotted) line represents the heaving (pitching) displacement.

5.1. *Coupled-mode flutter versus SDOF flutter*

In § 4.3, we analysed the flutter characteristics within the two-dimensional parameter space (k_h, k_α), and discovered six different aeroelastic phenomena. Among them, there are four types of flutter, including pitching instability within coupled-mode flutter, heaving instability within coupled-mode flutter, SDOF pitching flutter and SDOF heaving flutter.
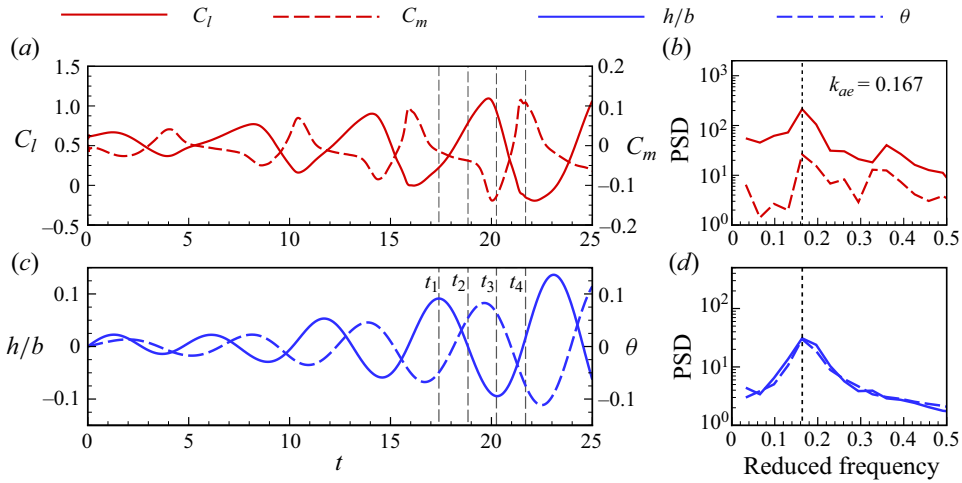
Figure 29. Heaving instability of coupled-mode flutter at P2: $k_h = 0.18$, $k_\alpha = 0.15$. (*a*) Force coefficients, (*c*) displacements, (*b*,*d*) PSD, $k_{ae} = 0.167 = 0.93k_h$.
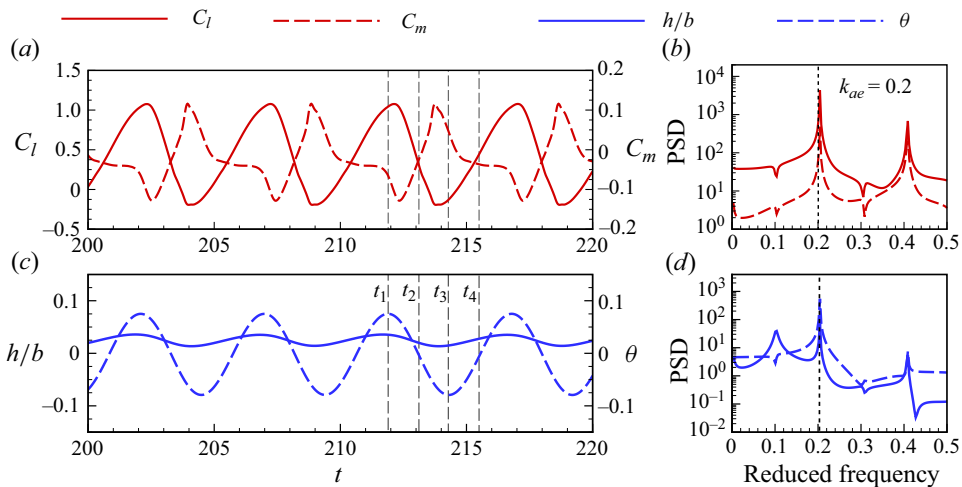

Figure 30. The SDOF pitching flutter at P3: $k_h = 0.1$, $k_\alpha = 0.2$. (*a*) Force coefficients, (*c*) displacements, (*b*,*d*) PSD, $k_{ae} = 0.2 = k_\alpha$.

They can be classified into two categories: coupled-mode flutter and SDOF flutter. The observed phenomena and their categorization are based on the frequency characteristics of unstable coupled modes predicted by the aeroelastic model. When the frequency of the unstable coupled mode is locked to its natural frequency, it is classified as an SDOF flutter. On the other hand, when the frequencies of the two coupled modes deviate from their natural frequencies and approach each other, it is considered a coupled-mode flutter. In order to verify the results of the aeroelastic model and to clarify the behaviour and characteristics of various flutters in the time-domain nonlinear response, we selected one state from each of the four types of flutter to demonstrate and analyse their time-domain responses obtained from CFD–CSD, as shown in figures 28–31, corresponding to points P1 to P4 in figure 27. The vertical axis range of figures 28–31 was set to the same value.
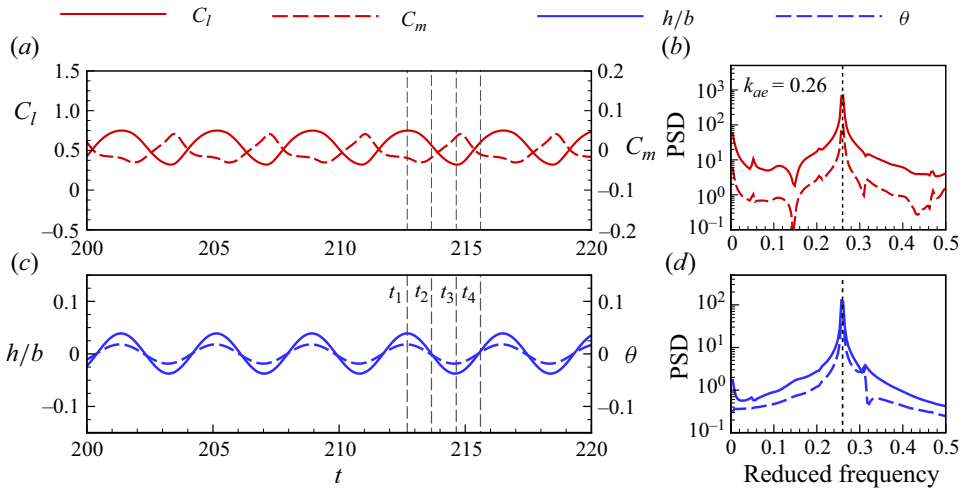
Figure 31. The SDOF heaving flutter at P4: $k_h = 0.26$, $k_\alpha = 0.31$. (*a*) Force coefficients, (*c*) displacement, (*b*,*d*) PSD, $k_{ae} = 0.26 = k_h$.

Figure 28 shows the time-domain response of the pitching instability with coupled-mode flutter at P1. Figure 29 depicts the time-domain response of the heaving instability within coupled-mode flutter at P2. For coupled-mode flutter, the amplitudes of force coefficients and displacements rapidly increase. This linear growth persists until the limit of the CFD–CSD method employed in this study, with the final obtained amplitudes before computational failure being $A_{h/b} > 1$ and $A_\theta > 0.6$. Figures 30 and 31 depict the time-domain response of the SDOF pitching (heaving) flutter in LCOs at P3 (P4), respectively. For SDOF flutter, the response of the aerodynamic forces and displacement eventually reach a LCO.

To more intuitively display these four types of flutter, we present the pressure and streamline diagrams at four typical moments for P1 to P4, as shown in figures 32–35. The horizontal dashed lines indicate the $y = 0$ position, assisting in illustrating the elastic deformation of the airfoil. The typical moments are divided into four equal parts of a full cycle of structural modal displacement, with P1 and P3 based on the pitching mode displacement, and P2 and P4 based on the heaving mode displacement.

For P1 and P2 states, both the pitching and heaving mode amplitudes are large, but their phase angles differ. When the pitching mode displacement of P1 is at its maximum (figure 32*a*), the heaving mode displacement is close to zero; conversely, when the heaving mode displacement is at its maximum (figure 32*b*), the pitching mode displacement is close to zero. The pattern for the P2 state is different: when the heaving mode displacement is at its maximum (figure 33*a*), the pitching mode displacement is also significant. For the P3 and P4 states, there is a significant difference in the displacement amplitudes of the pitching and heaving modes. The P3 state is dominated by pitching mode vibrations (figure 34), while the P4 state is dominated by heaving mode vibrations (figure 35). This pattern is more clearly illustrated in Lissajous figure 36, where there are evident differences in the vibration forms among the four states.

The time-domain responses of coupled-mode flutter and SDOF flutter exhibit many different characteristics, with the displacement response curve being more concise and exhibiting better regularity. Below, we extract various features of the displacement response curve for comparison. These features primarily include η_{ae}, amplitude ratio R_A

Figure 32. Pressure contours and streamlines in one period of pitching mode at P1: (*a*) t_1, (*b*) t_2, (*c*) t_3, (*d*) t_4.

Figure 33. Pressure contours and streamlines in one period of heaving mode at P2: (*a*) t_1, (*b*) t_2, (*c*) t_3, (*d*) t_4.
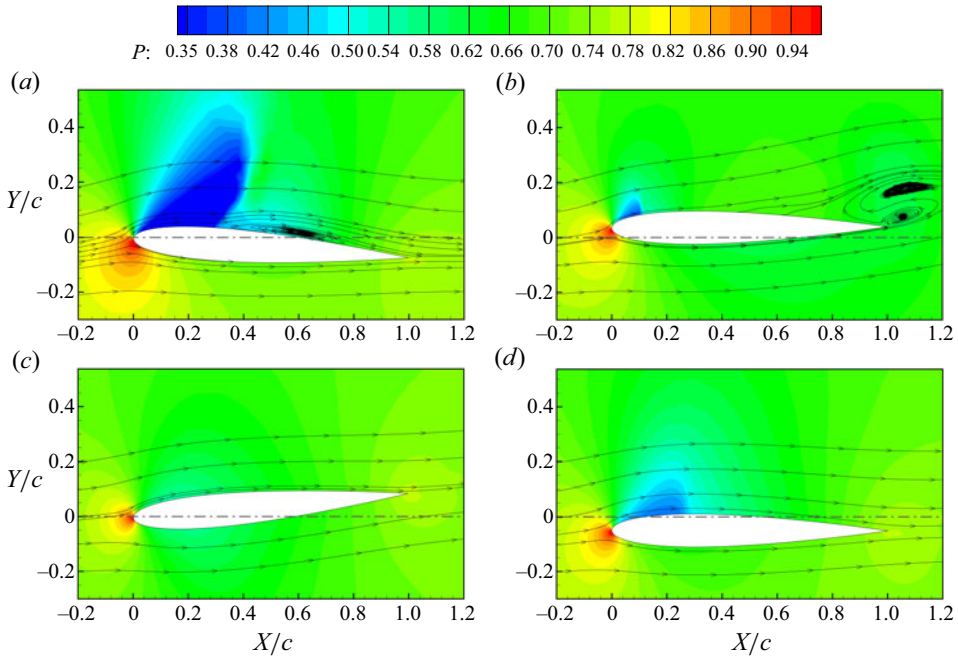
Figure 34. Pressure contours and streamlines in one period of pitching mode at P3: (*a*) t_1, (*b*) t_2, (*c*) t_3, (*d*) t_4.
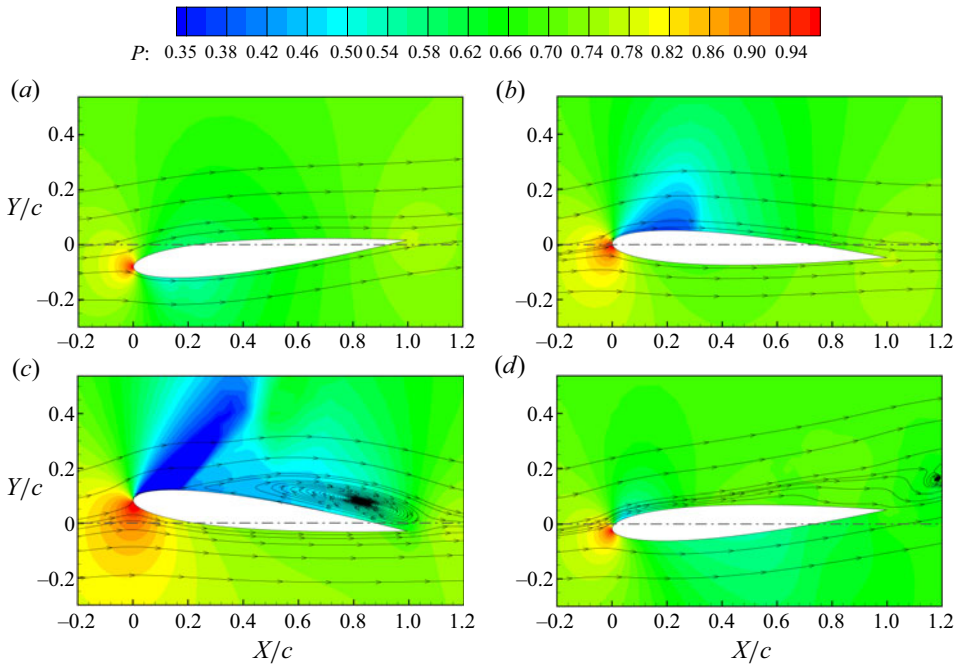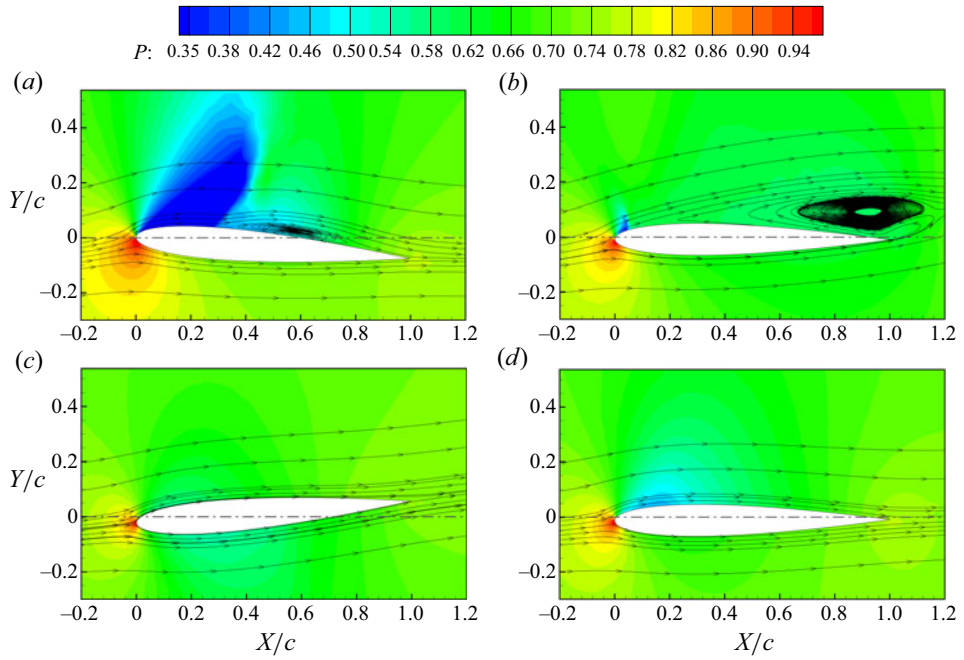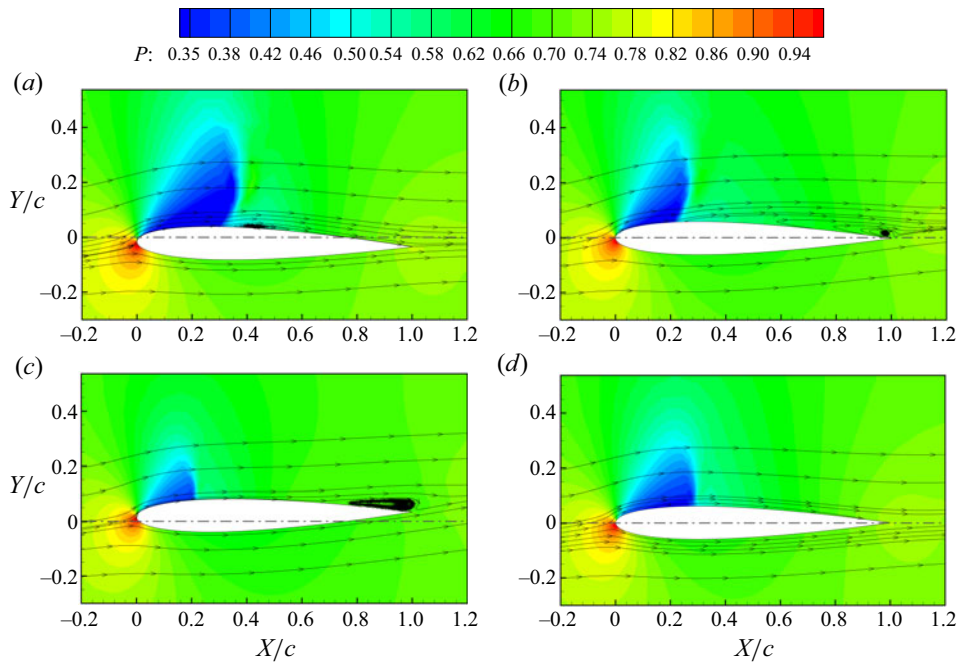

Figure 35. Pressure contours and streamlines in one period of heaving mode at P4: (*a*) t_1, (*b*) t_2, (*c*) t_3, (*d*) t_4.
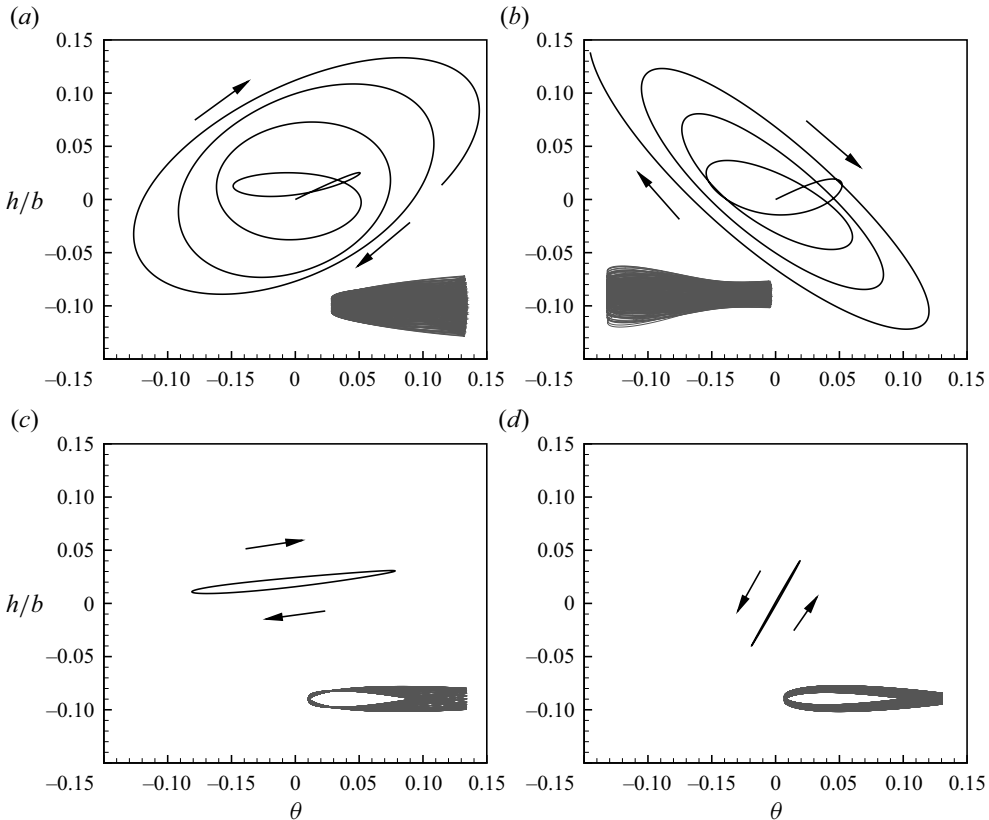
Figure 36. Lissajous figure of the pitching and heaving mode response and airfoil vibration range diagram: (*a*) P1, (*b*) P2, (*c*) P3, (*d*) P4.

and phase angle $\varphi_{\theta-h}$, as illustrated in (5.1):

$$
\left.
\begin{aligned}
\eta_{ae} &= |k_{ae} - k_\alpha|/|k_h - k_\alpha|, \\
R_A &= A_{h/b}/A_\theta, \\
\varphi_{h/b-\theta} &= \left| t_{max(h/b)} - t_{max(\theta)} \right|/(T_{ae}).
\end{aligned}
\right\}
\tag{5.1}
$$

The meanings of the parameters in (5.1) are shown in figure 37, where η_{ae} donates the deviating degree of the response frequency compared with the natural frequency of the unstable mode. When $\eta_{ae} = 1$, $k_{ae} = k_\alpha$. When $\eta_{ae} = 0$, $k_{ae} = k_h$. The amplitude of the non-dimensional heaving displacement is denoted by $A_{h/b}$, and the amplitude of the pitching angle (in radians) is represented by A_θ. The period of the response curve is denoted by T_{ae}, while $t_{max(\theta)}$ and $t_{max(h/b)}$ represent the non-dimensional time corresponding to the maximum pitching displacement and heaving displacement within the same period.

The features of the above four types of flutter are shown in table 2, where P1, P2, P3 and P4 represent pitching instability within coupled-mode flutter, heaving instability within coupled-mode flutter, SDOF pitching flutter and SDOF heaving flutter, respectively. For coupled-mode flutter, since the amplitude of the response curve keeps increasing, the features are extracted for each period within the range shown in figures 28 and 29,
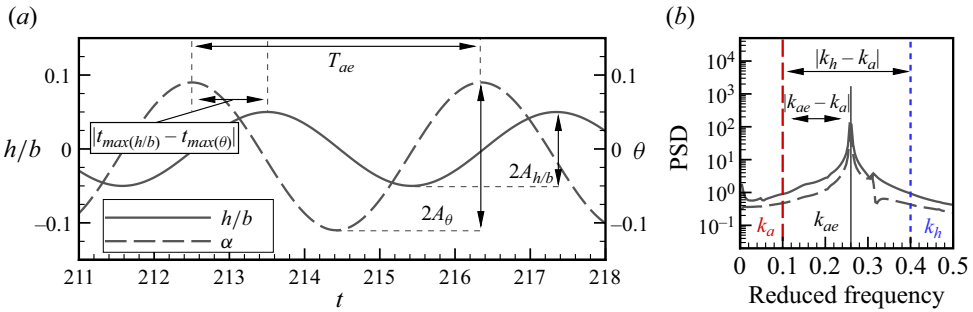
Figure 37. A schematic diagram illustrating the meanings of the parameters in (5.1). (*a*) Displacements and (*b*) PSD.

Point (k_h, k_α)	η_{ae}	R_A	$\varphi_{\theta-h}$		Flutter types	
P1 (0.136, 0.16)	0.42 (<0.5)	0.74 (<1)	0.16		Pitching instability of coupled-mode flutter	
P2 (0.18, 0.15)	0.57 (>0.5)	1.13 (>1)	0.38	($\gg$0)	Heaving instability of coupled-mode flutter	Coupled-mode flutter
P3 (0.1, 0.2)	0.00	0.15 (≪1)	0.04		SDOF pitching flutter	
P4 (0.26, 0.31)	1.00	2.09 ($\gg$1)	0.01	(≈0)	SDOF heaving flutter	SDOF flutter
P7 (0.24, 0.06)	($k_{ae} = k_b$)	3.12	—	—	Forced vibration	
P6 (0.05, 0.1)	—	—	—	—	Stable state	

Table 2. Various features of the displacement response of six aeroelastic phenomena.

and then averaged. For SDOF flutter, these features are directly extracted from the LCOs shown in figures 30 and 31.

For η_{ae} in table 2, it can be observed that at P1 and P2, their response frequencies lie between the natural frequencies of the structural modes, and they are closer to the unstable mode. On the other hand, the response frequencies at P3 and P4 are equal to the unstable structural mode natural frequencies. For R_A, both structural modes at P1 and P2 exhibit significant vibrations, with the ratio between them being close to one. Meanwhile, the values of R_A at P3 and P4 are significantly far from 1. Regarding $\varphi_{\theta-h}$, there is a noticeable phase lag between the heaving displacement and pitching displacement under P1 and P2 states, which is approximately 15 % to 40 % of the vibration period. In contrast, there is almost no phase difference between the two modes under P3 and P4 states, with the difference being less than 5 %. These differences and characteristics fully demonstrate that the aeroelastic phenomenon under P1 and P2 states corresponds to coupled-mode flutter, while the aeroelastic phenomenon under P3 and P4 states belongs to SDOF flutter. It should be noted that P4 indicates a specific SDOF heaving flutter. Here, $k_h = 0.26$, which is significantly higher than the flutter boundary for SDOF heaving airfoil (0, 0.138), as shown in figure 23. This special phenomenon has been analysed in § 4.1 by the aeroelastic model. The results of the CFD–CSD method confirm the accuracy of the aeroelastic model presented in this paper. The last two rows in table 2 also provide the eigenvalues at P7 and P6. State P7 represents a forced vibration state characterized by the dominant response frequency being equal to the frequency of the fluid mode. State P6 is a stable state where there is no periodic oscillation in the force coefficient and displacement response. The dynamical characteristics at P7 and P6 are discussed in detail in § 5.2.

999 A24-34

The phenomenon of SDOF flutter that arises in the aeroelastic system of a 2DOF airfoil is worthy of further discussion. This phenomenon has been commonly observed in previous transonic aeroelastic problems. It can be categorized into two types. The first one is just like the SDOF flutter that occurs on transonic buzz and the frequency lock-in in transonic buffeting flow. The fluid mode is coupled with a structural mode, leading to the instability of that structural mode. The addition or removal of another structural mode has minimal impact on this SDOF flutter system. The second type occurs in a transonic flutter. As *Ma*/AOA increases, the critical velocity of transonic flutter rapidly decreases. The system's basic vibration frequency shifts from being between the natural frequencies of mode A and mode B to almost aligning with the natural frequency of mode A. Mode A and mode B mentioned here are just used as examples. Significantly different from the first type, when mode B is eliminated, the second type of SDOF flutter will no longer occur. Dowell conducted a study on the transonic flutter of 2DOF airfoils based on numerical simulation methods (Kholodar *et al.* 2004). This study discovered and noted that: 'The flutter frequency at that point is essentially the same as the coupled in vacuo natural frequency corresponding to a dominant plunge motion. Correspondingly, the flutter eigenvector is dominated by the plunge motion. This is an example of single-DOF flutter, but note that the critical aeroelastic mode is a mass coupled natural mode, albeit one that is plunge dominated'. In the present results shown in figure 22, region I and the lower right corner of region II belong to the first type of SDOF flutter. The upper section of region II is the second type. We found that the second type of SDOF flutter, which involves flow, heaving and pitching modes deeply coupled, is a typical result. This type of flutter will not occur in the absence of any mode.

5.2. *Disappearance of SDOF flutter*

In figure 22, we observed that the SDOF flutter disappears due to coupling with another structural mode. This phenomenon can be categorized into two regions. The first one is the reduction in SDOF-pitching-flutter boundaries due to coupling with the heaving mode, occurring at ($i_n = k_h/k_\alpha = (0.3, 0.8)$, $k_\alpha = (0.3, 0.42)$). The second is that the SDOF heaving flutter disappears by the coupling with the pitching mode, happening at ($i_n = (0.3, 0.5)$, $k_\alpha = (0, 0.12)$). It is evident that the line with $k_h/k_\alpha = 0.5$ intersects these two regions, as depicted in figure 27. The subsequent analysis focuses on the root locus at $k_h/k_\alpha = 0.5$ to elucidate the underlying mechanism of this phenomenon, as illustrated in figure 38. The mode veering occurs between Branch 1 and Branch 3. Branch 2 consistently represents the pitching mode, and only Branch 2 exhibits an unstable region. At the instability region, the frequency of the coupled pitching mode locks onto the natural pitching frequency. Thus, it is defined as SDOF pitching flutter. The right flutter boundary of the 2DOF aeroelastic system is located at $k_\alpha = 0.35$. This is significantly lower than that ($k_\alpha = 0.42$) for an SDOF pitching airfoil, as shown in figure 39(*a,b*). In other words, at $k_h/k_\alpha = 0.5$, there is a reduction in the SDOF-pitching-flutter boundaries in the 2DOF aeroelastic system compared with an SDOF pitching airfoil. The left boundary of the 2DOF aeroelastic system is located at $k_\alpha = 0.12$, $k_h = 0.06$. For an SDOF heaving airfoil, the region of SDOF flutter is $k_h = (0, 0.138)$, as shown in figure 39(*c,d*). In other words, at $k_h/k_\alpha = 0.5$, compared with an SDOF heaving airfoil, the SDOF heaving flutter disappears in the 2DOF aeroelastic system. Since the frequency ratio of the 2DOF aeroelastic system is 0.5, the range of the horizontal axis in figure 39(*a,b*) has been set to $k_\alpha = (0, 0.5)$. The range of the horizontal axis in figure 39(*c,d*) has been set to $k_\alpha = (0, 0.25)$. This allows for a direct comparison between figures 39 and 38(*b,c*).
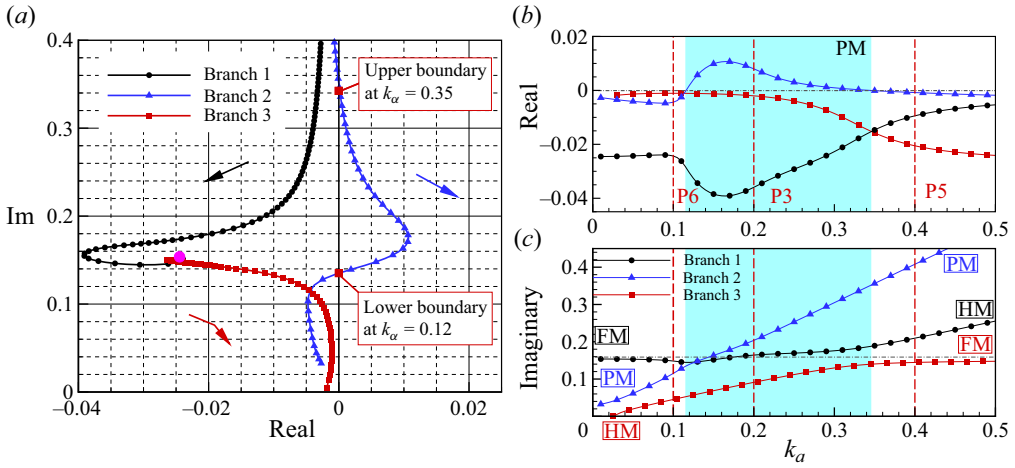
Figure 38. (*a*) Eigenvalue loci of the 2DOF aeroelastic system at $k_h/k_\alpha = 0.5$. (*b*) Real parts and (*c*) imaginary parts of the root loci changes with the natural pitching frequency.
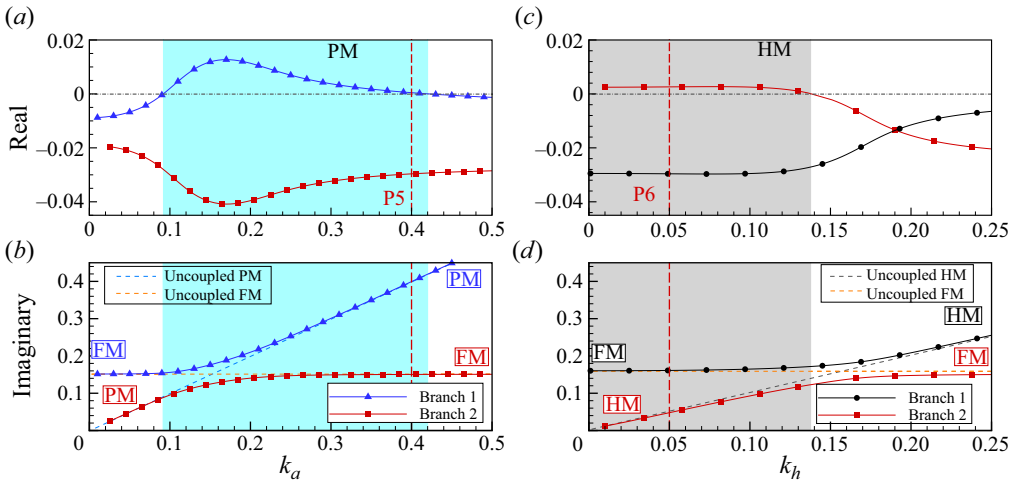

Figure 39. Real part and imaginary part of the root loci of the SDOF airfoil. (*a,b*) The SDOF pitching airfoil. (*c,d*) The SDOF heaving airfoil.

For the SDOF airfoils shown in figure 39, (2.2) and (2.3) degenerate into the following forms:

$$
\left.
\begin{aligned}
\text{SDOF heaving case:} \quad & \frac{\ddot{h}}{b} + k_h^2 \frac{h}{b} = \frac{1}{\pi\mu}(-C_l) \\
\text{SDOF pitching case:} \quad & \ddot{\theta} + k_\theta^2 \theta = \frac{1}{\pi\mu r_\theta^2}(2C_m),
\end{aligned}
\right\}
\tag{5.2}
$$

where $\mu = 200$, $r_a^2 = 1.036$. The free-stream conditions are $Ma = 0.7$, $Re = 3 \times 10^6$, $\alpha = 4.5°$.

The instability of aeroelastic systems can be attributed to the coupling between different modes. Specifically, in SDOF airfoils, the fluid mode is only coupled with a structural

999 A24-36

mode, leading to instability. On the contrary, 2DOF aeroelastic systems exhibit coupling among multiple modes including fluid, pitching and heaving modes. Due to the presence of an additional structural mode, the energy of the fluid mode is distributed across two structural modes, delaying the onset of instability and reducing its unstable region. For instance, in figure 39(a,b), the coupling between pitching and fluid modes results in instability of the coupled pitching mode at $k_\alpha = 0.42$. Meanwhile, in figure 39(c,d), near $k_h = 0.21$, corresponding to $k_\alpha = 0.42$, the natural frequencies of heaving mode and fluid mode become close, and mode veering occurs. In the 2DOF system, the mode veering between fluid mode and heaving mode weakens the ability of the fluid mode to induce instability of the pitching mode, thereby delaying the occurrence of SDOF pitching flutter. In figure 38(b,c), an ongoing SDOF pitching flutter inhibits the occurrence of SDOF heaving flutter in the range of $k_\alpha = (0.12, 0.35)$ and $k_h = (0.06, 0.175)$. In the range of $k_\alpha = (0, 0.12)$ and $k_h = (0, 0.06)$, the coupled pitching mode regains a stable state. However, the natural frequency of the pitching mode is closer to that of the fluid mode, which still suppresses the instability of the heaving mode, preventing SDOF heaving flutter. Therefore, under specific conditions, the release of other degrees of freedom can enhance aeroelastic stability. In conclusion, we have demonstrated that the coupling of different modes plays a crucial role in determining the stability of aeroelastic systems.

To further illustrate this point, we have performed CFD–CSD simulations for typical states denoted by the red vertical line (P5, P6) in figures 38 and 39, corresponding to figures 40 and 41. Compared with the flutter, the aerodynamic and displacement are stable at P5, as shown in figure 40. For the SDOF pitching airfoil, the pitching mode is unstable at $k_\alpha = 0.4$, and the vibration amplitude is large due to the SDOF pitching flutter, as depicted by the grey dotted line in figure 40. However, for the 2DOF aeroelastic system, the structural pitching mode remains stable due to the release of the heaving mode. Figure 41 shows the time-domain response at P6. The response amplitude is mainly due to the residual energy of the initial disturbance. For the SDOF heaving airfoil, the heaving mode is unstable at $k_h = 0.05$, and the vibration amplitude is large due to the SDOF heaving flutter, as depicted by the grey dotted line in figure 41. However, for the 2DOF aeroelastic system, the structural heaving mode remains stable due to the release of the pitching mode.

5.3. *Fluid mode instability induced by the elastic structure*

This section analyses the mechanism of phenomenon V – forced vibration – shown in figure 22. Existing research has found that elastic structures can cause a reduction in the transonic buffeting boundary ($Ma = 0.7$, $\alpha = 3.9°$) (Gao *et al.* 2018). A stability analysis based on a linear ROM was conducted on an SDOF pitching airfoil at $\mu = 60$, $Ma = 0.7$, $\alpha = 4.5°$, resulting in the root loci of the aeroelastic system as a function of the natural pitching frequency, as shown in figure 42(a,b). Only Branch 1 becomes unstable. Based on the relationship between the coupled frequency of Branch 1 and the natural frequencies of the structural/fluid modes, the dynamic modes are distinguished. At low pitching natural frequencies, it is forced vibration due to the instability of the dominant fluid mode; at high pitching natural frequencies, it is flutter due to the instability of the structural mode. This unique phenomenon is summarized as a reduction in the buffet boundary caused by the elastic structure.

A similar phenomenon was observed in the study of a 2DOF airfoil, as shown in figure 42(c,d). In the root locus at $\mu = 200$, $k_h/k_\alpha = 3$, only Branch 2 becomes unstable. Based on the relationship between the coupled frequency of Branch 2 and the natural
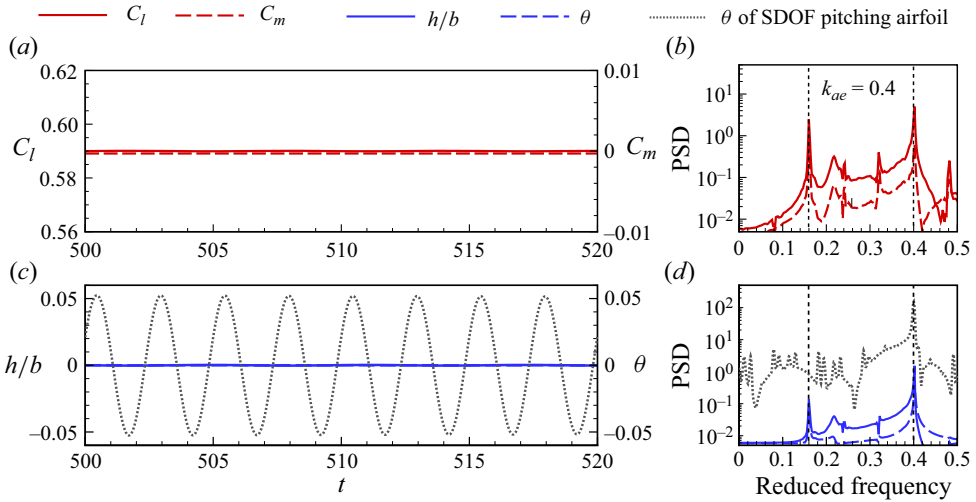
Figure 40. Stable state at P5: $k_h = 0.2$, $k_\alpha = 0.4$. (*a*) Force coefficients, (*c*) displacements, (*b,d*) PSD.
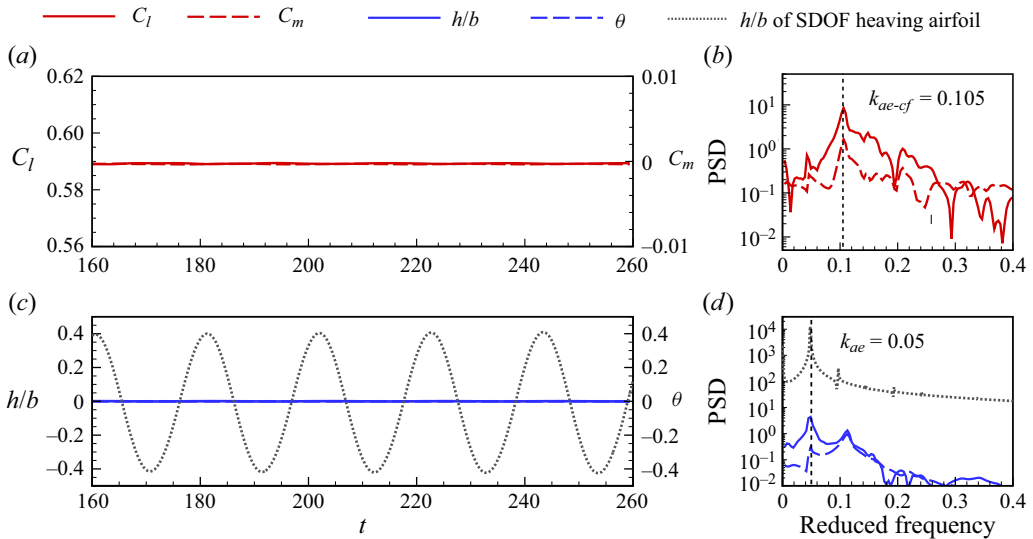

Figure 41. Stable state at P6: $k_h = 0.05$, $k_\alpha = 0.1$. (*a*) Force coefficients, (*c*) displacements, (*b,d*) PSD.

frequencies of the structural/fluid modes, three different types of dynamic modes were identified for this frequency ratio. The blue region at $k_\alpha = (0.15, 0.42)$ represents pitching mode instability, the red region at $k_\alpha = (0.05, 0.15)$ represents dominant fluid mode instability and the grey region at $k_\alpha = (0, 0.05)$ represents heaving mode instability. Consequently, it can be concluded that in the red region, the instability of the dominant fluid mode occurs. To further illustrate this point, we have performed CFD–CSD simulations for typical states denoted by the red vertical line (P7) in figure 42(*c,d*), as shown in figure 43. It can be observed that under this condition, the coupled frequency k_{ae} of the system is dominated by the buffeting frequency k_b, with the natural frequency of the structural mode completely dissipating, which verifies the aforementioned conclusion.
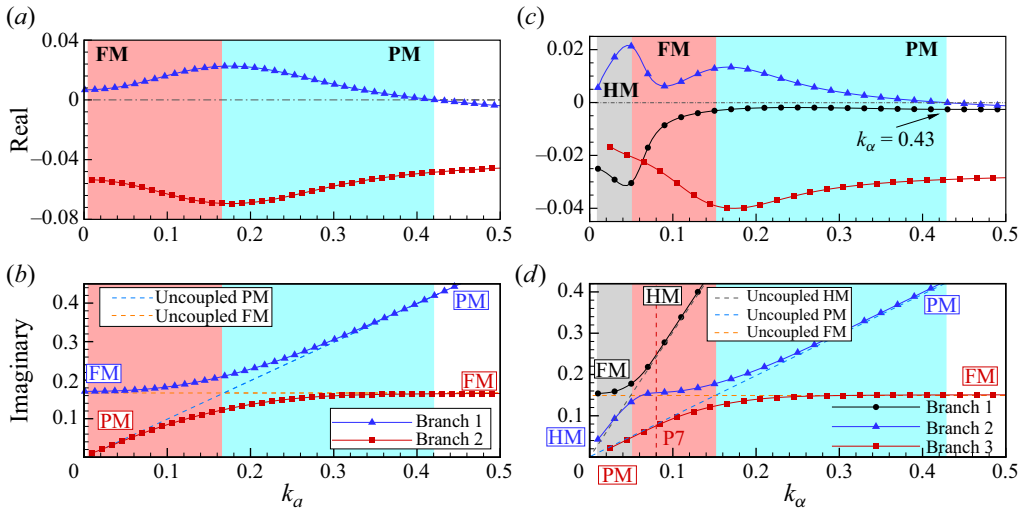
999 A24-38

Figure 42. Real part and imaginary part of the root loci change with the natural pitching frequency. (*a*,*b*) An SDOF pitching airfoil at $\mu = 60$, $Ma = 0.7$, $\alpha = 4.5°$ (Gao *et al.* 2018). (*c*,*d*) A 2DOF airfoil at $\mu = 200$, $k_h/k_\alpha = 3$.

6. Conclusions

In the present work, a ROM for transonic pre-buffet flow was constructed based on the identification technology. Coupling with the 2DOF structural equations, an efficient ROM-based flutter analysis method was formulated. Based on the aeroelastic model and the CFD–CSD coupling algorithm, flutter characteristics and types under representative frequency ratios were studied, accompanied by an analysis of the influence exerted by structural parameters. Within the two-dimensional parameter space defined by k_h and k_α, six distinct aeroelastic phenomena were identified and investigated. The main conclusions can be summarized as follows:

(1) The dominant fluid mode was identified for the 2DOF (heaving and pitching) airfoil at $Ma = 0.7$, $Re = 3 \times 10^6$, $\alpha = 4.5°$, with a dimensionless frequency of 0.155 and a negative growth rate of -0.026 (stable). The study revealed that the dominant fluid mode is directly related to the flutter types. The existence of the fluid mode transitions the transonic flutter type from coupled-mode flutter to SDOF flutter, which leads to a reduction in the flutter boundary.

(2) The six identified aeroelastic phenomena are SDOF heaving flutter, SDOF pitching flutter, heaving instability within coupled-mode flutter, pitching instability within coupled-mode flutter, forced vibration and stable state. There are three noteworthy points that merit discussion. First, SDOF heaving flutter occurs at high natural heaving frequencies ($i_n = k_h/k_\alpha = (0.8, 1)$, $k_h = (0.2, 0.4)$). Second, there is a reduction in SDOF-pitching-flutter boundaries due to the coupling of the heaving mode ($i_n = (0.3, 0.8)$, $k_\alpha = (0.3, 0.42)$). Third, at very low natural frequencies, SDOF heaving flutter disappears due to the coupling with the pitching mode, while all three major modes of the system remain stable ($i_n = (0.3, 0.5)$, $k_\alpha = (0, 0.12)$).

(3) The SDOF flutter that occurs in the aeroelastic system of a 2DOF airfoil can be classified into two types. The first type is similar to the SDOF flutter observed in transonic buzz and the frequency lock-in of transonic buffet. The addition or removal of another structural mode has minimal impact on this SDOF flutter system.
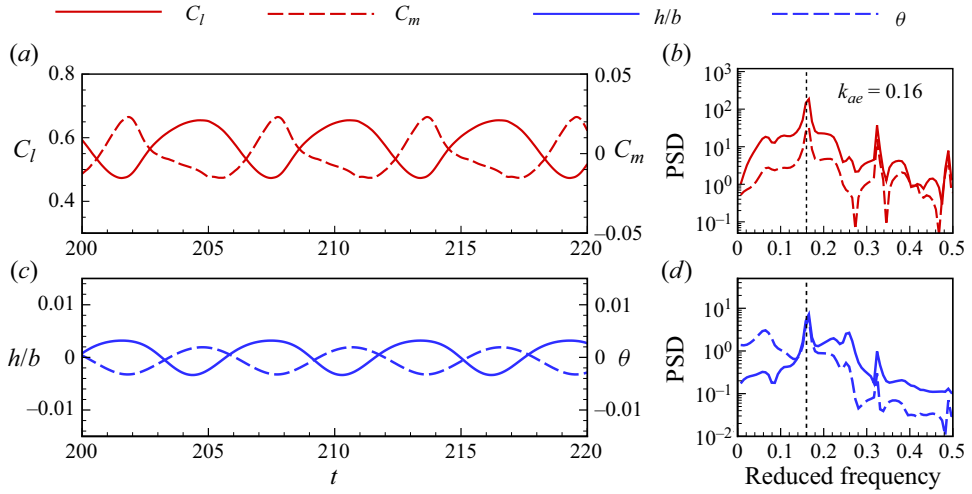
Figure 43. Forced vibration at P7: $k_h = 0.24$, $k_\alpha = 0.08$. (*a*) Force coefficients, (*c*) displacements, (*b*,*d*) PSD, $k_{ae} = 0.16 = k_b$.

The second type occurs in coupled-mode flutter. As *Ma*/AOA increases, the oscillation frequency of the system shifts from lying between the natural frequencies of two structural modes to almost aligning with the natural frequency of the unstable mode. Unlike the first type, the second type of SDOF flutter is characterized by strong coupling dominated by the unstable mode. It results from the interaction among the flow, heaving and pitching modes, and does not occur in the absence of any mode.

Future research can explore the following aspects. The qualitative analysis provided in this study outlines how the dominant fluid mode influences transonic flutter and how coupling with other structural modes affects transonic buzz (SDOF flutter). However, further investigation is needed to achieve a quantitative analysis of the impact of these modes. As outlined in §4.2, the boundaries between different aeroelastic phenomena are currently determined empirically, despite the transition being continuous rather than discrete. To enable a quantitative and gradual analysis of various aeroelastic phenomena, additional analytical methods may be of help.

Declaration of interests. The authors report no conflict of interest.

Author ORCIDs.
- Zihao Dou https://orcid.org/0000-0002-4611-5044;
- Chuanqiang Gao https://orcid.org/0000-0002-8674-7759;
- Weiwei Zhang https://orcid.org/0000-0001-7799-833X.

Appendix A. Nomenclature

CFD	Computational fluid dynamics
CSD	Computational structural dynamics
ARX	Autoregressive with exogenous input
ROM	Reduced-order model

PSD	Power spectrum density
SDOF	Single degree of freedom
2DOF	Two degrees of freedom
HM	Structural heaving mode
PM	Structural pitching mode
FM	Fluid mode
Ma	Mach number [1]
Re	Reynolds number [1]
c	Chord length [m]
b	Half-chord length [m]
t	Non-dimensional time [1]
α	Equilibrium angle of attack [deg.]
h/b	Non-dimensional heaving displacement [1]
θ	Pitching angle [rad]
C_l	Lift coefficient [1]
C_m	Pitching moment coefficient [1]
p	Non-dimensional pressure [1]
C_p	Pressure coefficient [1]
ρ	Density of free stream [kg m^{-3}]
U_∞	Velocity of free stream [m s^{-1}]
μ	Mass ratio [1]
a	Position of the elastic axis [1]
x_a	Static unbalance of the airfoil [1]
r_a	Gyration radius of the airfoil [1]
V^*	Non-dimensional velocity [1]
ω	Natural frequency [rad s^{-1}]
k	Reduced frequency [1]
k_h	Non-dimensional natural heaving frequency [1]
k_α	Non-dimensional natural pitching frequency [1]
i_n	Ratio of the natural frequencies of heaving and pitching modes [1]
k_b	Non-dimensional buffeting frequency [1]
k_{ae}	Dominant frequency of the response of the coupled system [1]
na, nb	Delay orders of the ARX model [1]
g	Growth rate [1]
A_θ	Amplitude of the pitching angle [rad]
$A_{h/b}$	Amplitude of the heaving displacement [1]
R_A	Ratio of the response amplitude of heaving and pitching modes [1]
η_{ae}	Deviating degree of the response frequencies [1]
$\varphi_{\theta-h}$	Phase angle of the response of heaving and pitching modes [1]

Appendix B. Validation of numerical methods and convergence of aeroelastic case

As the data source and validation method for the aeroelastic model in this paper, the accuracy and convergence of the CFD–CSD numerical method are crucial to ensuring the validity of the paper's results. Therefore, this appendix will briefly introduce the verification of the numerical method from three aspects: B.1, verification of CFD simulation accuracy for transonic buffet; B.2, convergence of the grid and the time step; B.3, verification of transonic flutter boundaries.
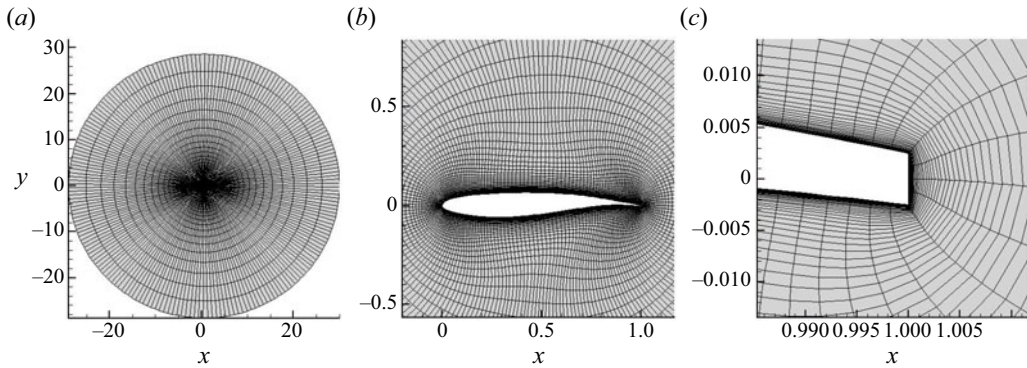
Figure 44. (*a*) Overall mesh diagram, (*b*) local detail map and (*c*) trailing-edge close-up.

	Turbulence models	Numerical schemes	α	ΔC_l	k_b
CFD	S-A	ROE	$3.5°$	0.9–1.08	0.215
		AUSM	$3.5°$	0.88–1.1	0.21
		AUSM	$3.7°$	0.86–1.12	0.22
	SST	ROE	$3.5°$	0.9–1.14	0.265
		AUSM	$3.5°$	0.93–1.14	0.287
		AUSM	$3.7°$	0.91–1.16	0.286
Exp.		—	$3.5°$	—	0.21

Table 3. The amplitude and frequency of lift coefficient in buffeting flow under different combinations of turbulence models and numerical schemes, compared with experiment (Exp.).

B.1. *Verification of CFD simulation accuracy for transonic buffet*

An OAT15A supercritical airfoil was adopted as an experimental model in the state of $Ma = 0.73$, $Re = 3 \times 10^6$, $\alpha = 3.5°$ by Jacquin *et al.* (2009), providing plenty of experimental data, particularly buffet loads. Therefore, a simulation is conducted based on this airfoil to verify the efficiency of the CFD solver in predicting buffet loads.

We first conducted a sensitivity study of the turbulence model and numerical schemes. The grid uses structured meshing and is stored in unstructured data format. The far-field boundary is 30 chord lengths away, and the first cell height of the boundary layer is $5 \times 10^{-6}c$, with a non-dimensional wall distance of $y \approx 1$, as shown in figure 44. The grid consists of 37 145 cells, and the physical time step for the unsteady calculations is 2×10^{-4} s. Table 3 compares the amplitude and frequency of the flutter lift coefficient response under different combinations of turbulence models and numerical schemes, with the calculation conditions set to $Ma = 0.73$, $Re = 3 \times 10^6$, $\alpha = 3.5°$. The comparison reveals that the turbulence model has a significant impact on the calculation results, whereas the influence of the numerical schemes is relatively small. The SST model predicts larger flutter loads and frequencies, which aligns with the conclusions from the literature. Compared with experimental results, the flutter frequency calculated using the S-A turbulence model aligns better with the experimental data. Therefore, for this airfoil flutter case, the S-A turbulence model and AUSM spatial discretization scheme are used in subsequent calculations.

Figure 45 shows the root-mean-square values of the pressure fluctuation on the upper profile surface, where Q_0 is the free-stream dynamic pressure. Wall pressure fluctuations
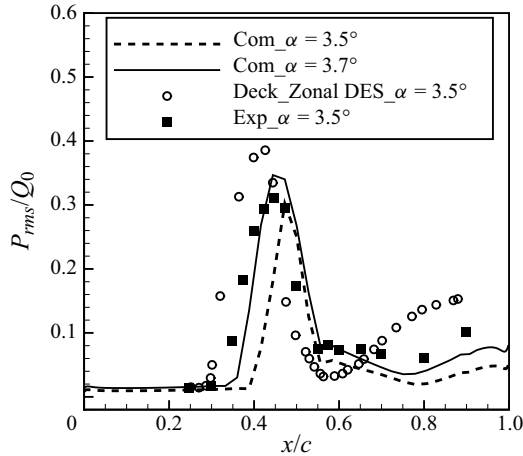
Figure 45. Influence of the incidence on the chordwise distribution of the root-mean-square surface pressure.
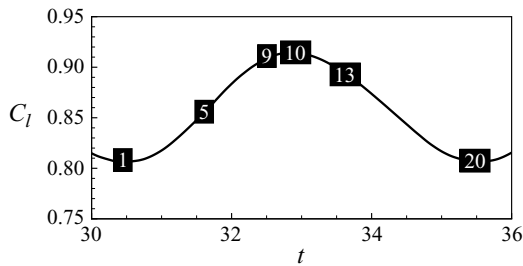

Figure 46. Schematic map of phases in one period of the shock motion.

are induced by the separated flow unsteadiness. The peak is related to the shock motion. In the present calculation, the predicted peak at $\alpha = 3.5°$ is slightly lower than the experimental one, whereas the calculated peak at $\alpha = 3.7°$ indicates better agreement. The result simulated by Deck (2005) using Zonal-DES at $\alpha = 3.5°$ shows a higher peak. That is, loads predicted by the S-A turbulence model are slightly smaller than those of the experiment. In the experiment of Jacquin *et al.* (2009), the model was a blunt trailing edge, whereas it was sharp in Deck's calculation (Deck 2005). In current simulations, both models are adopted and they exhibit nearly consistent results. Results provided in this paper are based on the sharp model.

Profiles of the velocity phase average measured at 60 % chord are provided in the study of Jacquin *et al.* (2009). These profiles show that buffet leads to the periodic separation of the boundary layer and the periodic shock motion. A schematic map of the phases is shown in figure 46. Phase 1 is when the shock is in the upstream location. Figure 47 displays the velocity contours and the velocity profiles at different phases in the upper surface location of $X/c = 0.6$, where y_s is the coordinate of the upper surface. In those computations, the boundary layer is attached at phase 5 (figure 47*b*), and the separation occurs at phase 9 (figure 47*c*). In the given four phases, velocity profiles of experiments agree well with those of calculations.
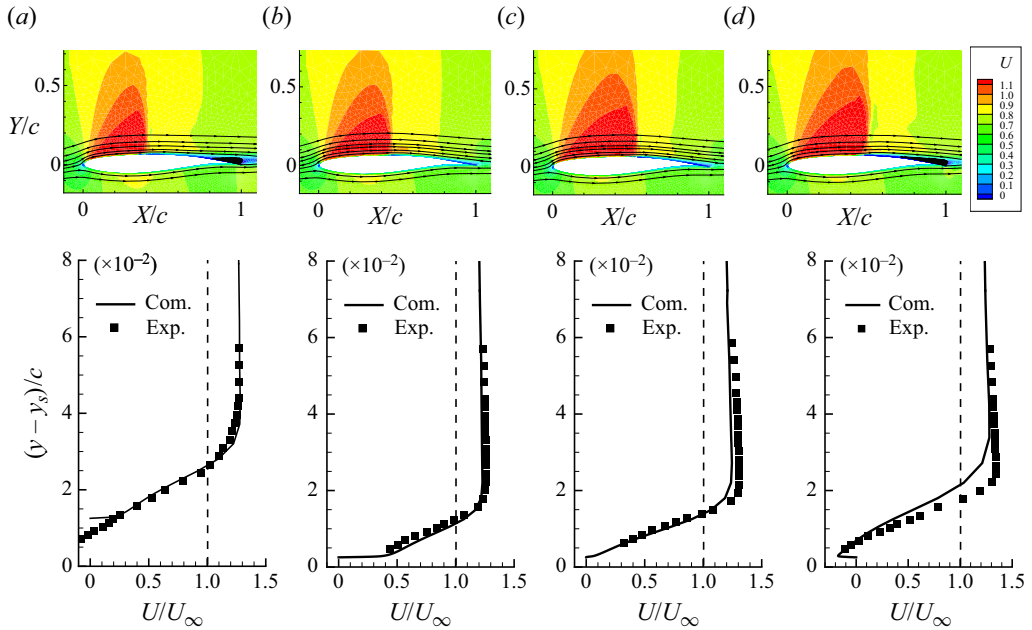
Figure 47. Non-dimensional velocity profiles of four phases in one period at $X/c = 0.6$, $Ma = 0.73$, $Re = 3 \times 10^6$, $\alpha = 3.7°$. (*a*) Phase 1, $X_{SW}/c = 0.39$. (*b*) Phase 5, $X_{SW}/c = 0.45$. (*c*) Phase 9, $X_{SW}/c = 0.54$. (*d*) Phase 13, $X_{SW}/c = 0.50$.

	G1	G2	G3	G4
Airfoil nodes	90	180	400	600
Surface nodes	4426	9624	25 361	43 004
Amplitude of C_l	0.080	0.100	0.110	0.110
Amplitude of C_m	0.016	0.024	0.024	0.024
Reduced frequency	0.183	0.181	0.180	0.180

Table 4. Dependence of the results on various grids differing in their spatial resolution.

B.2. *Convergence of the grid and the time step*

In order to assess convergence in numerical results, the transonic buffet flow at $Ma = 0.7$, $Re = 3 \times 10^6$, $\alpha = 5.0°$ has been computed for four grids G1 to G4 differing in their spatial resolution. All results presented in the present study are from grid G3, which is shown in figure 48. Results are detailed in table 4 for nodes of grids and the amplitude of aerodynamic forces, which shows that nearly all constants are converged down to the third digit. Results of grids G3 and G4 are almost equal, but the time cost of grid G3 is less. Therefore, grid G3 is adopted in this research considering the balance between efficiency and accuracy.

Generally, the time step of fluid dynamics is smaller than that of structural dynamics. Therefore, the time step of the present study is decided by the simulation of the buffet flow. For the time convergence of the buffet flow, simulations were run using non-dimensional computational time steps dt ranging from 0.02 to 1, where the physical time step is defined as d$t = dt_{physics} a_\infty / c$. Table 5 shows the aerodynamic forces, along with the
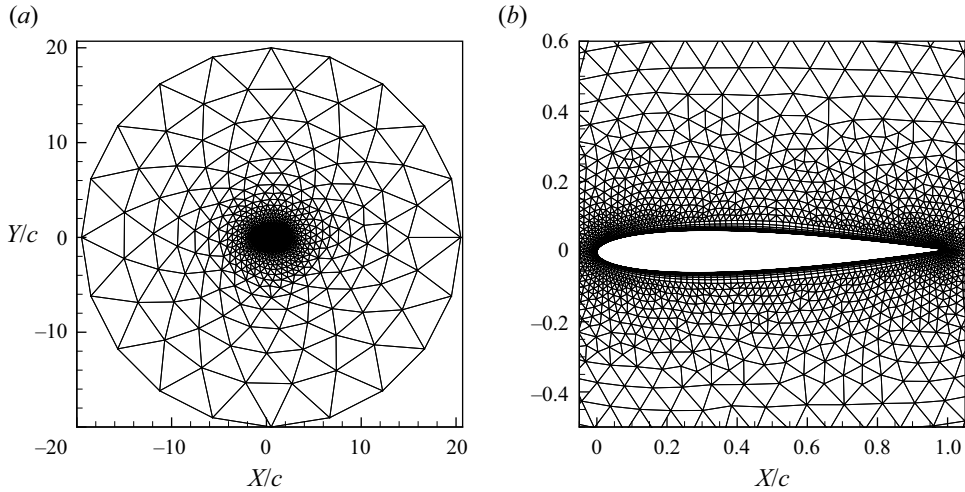
999 A24-44

Figure 48. The NACA0012 airfoil computational grid. (*a*) Overview of the grid. (*b*) Close-up view of the airfoil.

Non-dimensional dt	0.7	0.5	0.1	0.02
Physical dt (s)	2.06×10^{-3}	1.47×10^{-3}	2.94×10^{-4}	5.89×10^{-5}
Time-averaged C_l	0.540	0.574	0.576	0.577
Amplitude of C_l	0.09	0.108	0.110	0.110
Time-averaged C_m	0.146	0.154	0.156	0.156
Amplitude of C_m	0.012	0.024	0.024	0.024
Reduced frequency	0.16	0.178	0.180	0.180

Table 5. Comparison of results at different time steps.

reduced frequency using grid G3. When the time step increases to 1.0 or larger, the CFD solver cannot calculate a buffet. The results converge with a decreasing time step, and a non-dimensional time step no larger than 0.1 (physical time step of 0.00029 s) is adequate for present simulations.

Finally, we further verify the accuracy and convergence of the selected grid G3 and non-dimensional time step d$t = 0.1$ by comparing with experimental results in two aspects: the aerodynamic response under forced oscillation and its surface pressure distribution.

For the aerodynamic response under forced oscillation, the CT5 case with a large oscillation amplitude and a strong shock wave in the AGARD report 702 (NACA0012 airfoil) (Landon 1982) are carried out. The sinusoidal pitching motion of the airfoil is given in terms of the AOA as a function of time:

$$\theta(t) = \alpha + \theta_F \sin(2\pi \cdot k_p t), \tag{B1}$$

where α is the mean AOA; θ_F is the maximum pitching amplitude with respect to the mean; and k_p is the reduced frequency of the forced motion. The pitching axis and the moment integral point are both located at $0.25c$. Important parameters are as follows: $Ma = 0.755$, $Re = 5.5 \times 10^6$, $k_p = 0.0814$, $\alpha = 0.016°$, $\theta_F = 2.51°$.
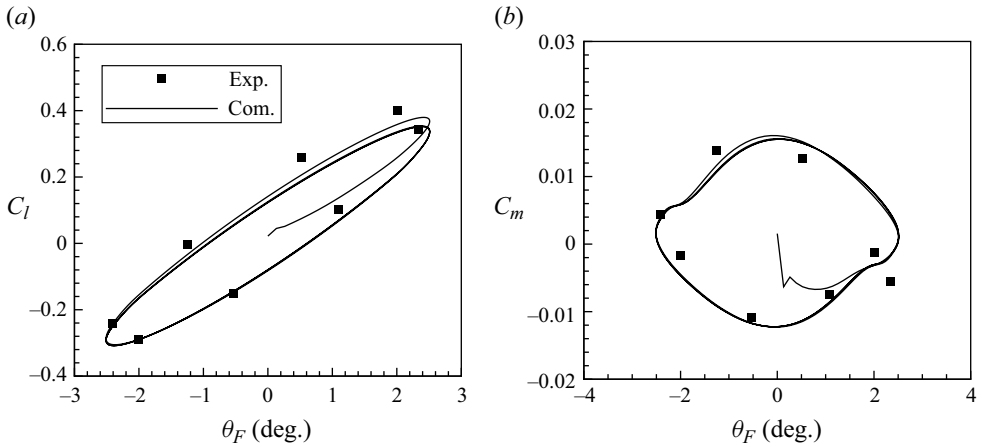
(*a*)

(*b*)

Figure 49. Comparison between numerical and experimental results from the AGARD CT5 case: (*a*) C_l and (*b*) C_m.
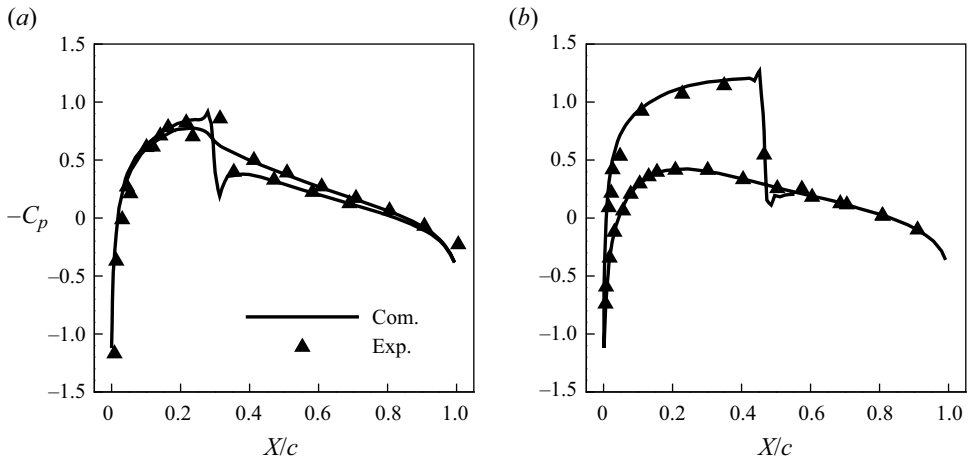
(*a*)

(*b*)

Figure 50. Comparison of surface pressure coefficient curves between CFD method and experimental results at different AOA during forced pitching oscillations: (*a*) $\theta = 1.09°$ upward motion and (*b*) $\theta = 2.01°$ downward motion.

Figure 49 shows both the numerical and experimental C_l and C_m results as a function of the instantaneous AOA. Numerical results reasonably match experimental data. Figure 50 shows a comparison of surface pressure coefficient curves between the CFD method and experimental results at different AOA during forced pitching oscillations. The high degree of agreement between the simulation and experimental results indicates that the CFD method used in this study can accurately describe unsteady flow effects and precisely calculate the aerodynamic loads during transonic unsteady shock wave motion.

B.3. *Verification of transonic flutter boundaries*

Due to the limited availability of detailed aeroelastic response data and the higher sensitivity of transonic aeroelastic responses to initial conditions and other parameters, direct comparisons of specific time-domain responses are rare. This study focuses on
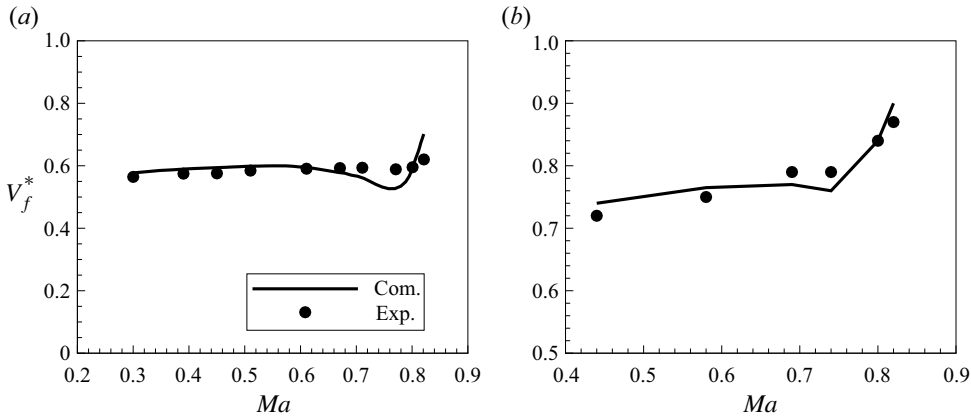
999 A24-46

Figure 51. Computed flutter boundary compared with the experimental data. (*a*) The BACT model. (*b*) The BSCW model.

aeroelastic stability issues, with an emphasis on the stability boundary. By comparing critical characteristics, we can partially verify the effectiveness of unsteady response calculations. Therefore, we choose the BACT (Rivera *et al.* 1992) and BSCW (Dansberry *et al.* 1993) cases to validate the CFD–CSD method. Relevant parameters of the BACT case are $\mu = 1139{-}4162$, $r_a^2 = 1.036$, $\alpha = 0°$ and $\omega_h/\omega_\alpha = 0.6539$ based on NACA0012 airfoil; these of the BSCW case are $\mu = 253{-}815$, $r_a^2 = 1$, $\alpha = 0°$ and $\omega_h/\omega_\alpha = 0.6324$ based on SC20414 airfoil. Details of other parameters can be found in studies by Rivera *et al.* (1992) and Dansberry *et al.* (1993). Figure 51 shows the computed flutter boundary of the BACT model and the BSCW model compared with the experimental data. For the two transonic flutter benchmark models mentioned above, the flutter boundaries obtained using our simulation method show good agreement with experimental results, validating the effectiveness of our CFD–CSD method.

Appendix C. Convergence of linear ROM and fluid modes

This appendix analyses the convergence of the modelling method and the characteristics of fluid modes from two aspects: C.1, convergence of the linear aeroelastic ROM; C.2, variation of fluid modes with AOA.

C.1. *Convergence of the linear aeroelastic ROM*

Based on four aeroelastic analysis models with delay orders ranging from 10 to 40, we analysed the eigenvalue roots of the coupled system at a frequency ratio of 0.85. As shown in figure 52, the main eigenvalue roots of the system exhibit a convergence trend as the delay order increases. The position of the eigenvalue representing the dominant fluid mode changes most significantly, showing convergence consistent with the pure aerodynamic model results, as shown in figure 27. The eigenvalues representing the structural modes show little overall change and also converge as the delay order increases. Therefore, the aeroelastic linear ROM in this paper demonstrates convergence with respect to the modelling delay order.
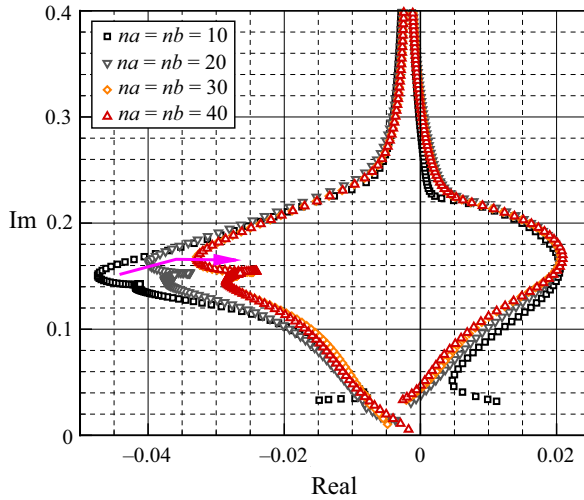
Figure 52. Eigenvalue loci of the aeroelastic system with delay orders ranging from 10 to 40 at $k_h/k_\alpha = 0.85$.
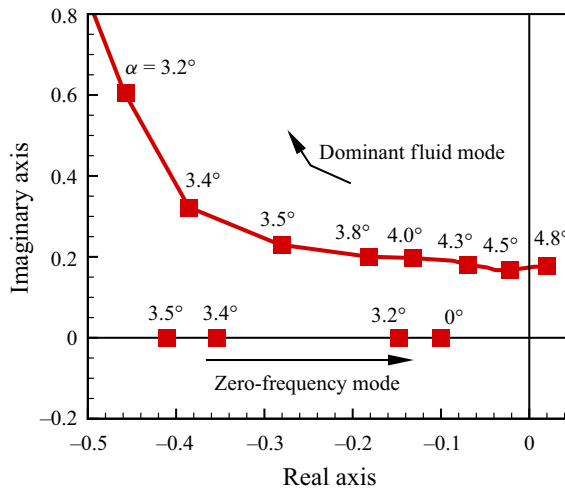

Figure 53. The variation of eigenvalues of the aerodynamic models with the AOA.

C.2. *Variation of fluid modes with AOA*

This section analyses the variation of fluid modes with the AOA. As shown in figure 53, using $\alpha = 4.5°$ as a reference, when α increases, the dominant fluid mode crosses the imaginary axis, and its growth rate changes from negative to positive, explaining the onset of buffet from a linear mode perspective. When α decreases, it can be observed that the damping of the dominant fluid mode increases rapidly and becomes greater than the zero-frequency mode at $\alpha = 3.4°$. Subsequently, the frequency of this mode also increases rapidly, while the zero-frequency mode stabilizes at a growth rate of approximately -0.1. This phenomenon shows that a decrease in the AOA increases the damping and frequency of the dominant fluid mode, eventually transforming it into one of several non-convergent numerical modes, meaning the dominant fluid mode disappears. Meanwhile, the damping of the zero-frequency mode gradually decreases and eventually takes over the position of

999 A24-48

the dominant fluid mode. However, the physical significance of the zero-frequency mode requires further investigation.

REFERENCES

AHN, H.T. & KALLINDERIS, Y. 2006 Strongly coupled flow/structure interactions with a geometrically conservative ale scheme on general hybrid meshes. *J. Comput. Phys.* **219** (2), 671–696.

BADCOCK, K.J., TIMME, S., MARQUES, S., KHODAPARAST, H., PRANDINA, M., MOTTERSHEAD, J.E., SWIFT, A., DA RONCH, A. & WOODGATE, M.A. 2011 Transonic aeroelastic simulation for instability searches and uncertainty analysis. *Prog. Aerosp. Sci.* **47** (5), 392–423.

BAI, C.-Y. & WU, Z.-N. 2017 Size and shape of shock waves and slipline for Mach reflection in steady flow. *J. Fluid Mech.* **818**, 116–140.

BENDIKSEN, O.O. 2011 Review of unsteady transonic aerodynamics: theory and applications. *Prog. Aerosp. Sci.* **47** (2), 135–167.

CHENG, Z., LIEN, F.-S., DOWELL, E.H., YEE, E., WANG, R. & ZHANG, J.H. 2023 Critical effect of fore-aft tapering on galloping triggering for a trapezoidal body. *J. Fluid Mech.* **967**, A18.

CHWALOWSKI, P., MASSEY, S.J., JACOBSON, K., SILVA, W.A. & STANFORD, B. 2022 Progress on transonic flutter and shock buffet computations in support of the third aeroelastic prediction workshop. *AIAA SciTech 2022 Forum*.

CROUCH, J.D., GARBARUK, A., MAGIDOV, D. & TRAVIN, A. 2009 Origin of transonic buffet on aerofoils. *J. Fluid Mech.* **628**, 357–369.

DANSBERRY, B., DURHAM, M., BENNETT, R., RIVERA, J., SILVA, W., WIESEMAN, C. & TURNOCK, D. 1993 Experimental unsteady pressures at flutter on the supercritical wing benchmark model. In *34th Structures, Structural Dynamics and Materials Conference*, p. 1592.

DECK, S. 2005 Numerical simulation of transonic buffet over a supercritical airfoil. *AIAA J.* **43** (7), 1556–1566.

DOERFFER, P., HIRSCH, C., DUSSAUGE, J.-P., BABINSKY, H. & BARAKOS, G.N. 2010 *Unsteady Effects of Shock Wave Induced Separation*, vol. 114. Springer Science & Business Media.

DOWELL, E. 2010 Some recent advances in nonlinear aeroelasticity: fluid-structure interaction in the 21st century. In *51st AIAA/ASME/ASCE/AHS/ASC Structures, Structural Dynamics, and Materials Conference 18th AIAA/ASME/AHS Adaptive Structures Conference 12th*, p. 3137.

DOWELL, E.H 2014 *A Modern Course in Aeroelasticity*, vol. 217. Springer.

DOWELL, E.H. 2024 Coupled-mode versus single-degree-of-freedom flutter: the third parameter in flutter. *AIAA J.* **62** (2), 864–868.

GAO, C., LIU, X. & ZHANG, W. 2021 On the dispersion mechanism of the flutter boundary of the AGARD 445.6 wing. *AIAA J.* **59** (7), 2657–2669.

GAO, C. & ZHANG, W. 2020 Transonic aeroelasticity: a new perspective from the fluid mode. *Prog. Aerosp. Sci.* **113**, 100596.

GAO, C., ZHANG, W., KOU, J., LIU, Y. & YE, Z. 2017*a* Active control of transonic buffet flow. *J. Fluid Mech.* **824**, 312–351.

GAO, C., ZHANG, W., LI, X., LIU, Y., QUAN, J., YE, Z. & JIANG, Y. 2017*b* Mechanism of frequency lock-in in transonic buffeting flow. *J. Fluid Mech.* **818**, 528–561.

GAO, C., ZHANG, W. & YE, Z. 2016*a* A new viewpoint on the mechanism of transonic single-degree-of-freedom flutter. *Aerosp. Sci. Technol.* **52**, 144–156.

GAO, C., ZHANG, W. & YE, Z. 2016*b* Numerical study on closed-loop control of transonic buffet suppression by trailing edge flap. *Comput. Fluids* **132**, 32–45.

GAO, C., ZHANG, W. & YE, Z. 2018 Reduction of transonic buffet onset for a wing with activated elasticity. *Aerosp. Sci. Technol.* **77**, 670–676.

GRIFFITHS, L.M., GAITONDE, A.L., JONES, D.P. & FRISWELL, M.I. 2018 Updating of aerodynamic reduced order models generated using computational fluid dynamics. *Proc. Inst. Mech. Engrs* **232** (9), 1739–1763.

HALDER, R., DAMODARAN, M. & KHOO, B.C. 2020*a* Deep learning based reduced order model for airfoil-gust and aeroelastic interaction. *AIAA J.* **58** (10), 4304–4321.

HALDER, R., DAMODARAN, M. & KHOO, B.C. 2020*b* Signal interpolation augmented linear nonintrusive reduced-order model for aeroelastic applications. *AIAA J.* **58** (1), 426–444.

HARTMANN, A., KLAAS, M. & SCHRÖDER, W. 2013 Coupled airfoil heave/pitch oscillations at buffet flow. *AIAA J.* **51** (7), 1542–1552.

HE, S., YANG, Z. & GU, Y. 2016 Limit cycle oscillation behavior of transonic control surface buzz considering free-play nonlinearity. *J. Fluids Struct.* **61**, 431–449.

HEEG, J., CHWALOWSKI, P., RAVEH, D.E., DALENBRING, M.J. & JIRASEK, A. 2015 Plans and example results for the 2nd AIAA aeroelastic prediction workshop. In *56th AIAA/ASCE/AHS/ASC Structures, Structural Dynamics, and Materials Conference*, p. 0437.

HOUTMAN, J. & TIMME, S. 2023 Global stability analysis of elastic aircraft in edge-of-the-envelope flow. *J. Fluid Mech.* **967**, A4.

ISOGAI, K. 1981 Transonic dip mechanism of flutter of a sweptback wing. *AIAA J.* **19**, 1240–1242.

JACQUIN, L., MOLTON, P., DECK, S., MAURY, B. & SOULEVANT, D. 2009 Experimental study of shock oscillation over a transonic supercritical profile. *AIAA J.* **47** (9), 1985–1994.

JAMESON, A. 1991 Time dependent calculations using multigrid, with applications to unsteady flows past airfoils and wings. In *10th Computational Fluid Dynamics Conference*, p. 1596.

KARNICK, P.T. & VENKATRAMAN, K. 2017 Shock–boundary layer interaction and energetics in transonic flutter. *J. Fluid Mech.* **832**, 212–240.

KHOLODAR, D.B., DOWELL, E.H., THOMAS, J.P. & HALL, K.C. 2004 Improved understanding of transonic flutter: a three-parameter flutter surface. *J. Aircraft* **41** (4), 911–917.

KORTHÄUER, T., ACCORINTI, A., SCHARNOWSKI, S. & KÄHLER, C.J. 2023 Experimental investigation of transonic buffeting, frequency lock-in and their dependence on structural characteristics. *J. Fluids Struct.* **122**, 103975.

KOU, J., ZHANG, W., LIU, Y. & LI, X. 2017 The lowest Reynolds number of vortex-induced vibrations. *Phys. Fluids* **29** (4), 041701.

LANDON, R.H. 1982 NACA 0012 oscillatory and transient pitching. *AGARD report* 702, pp. 45–59.

LI, X., LYU, Z., KOU, J. & ZHANG, W. 2019 Mode competition in galloping of a square cylinder at low Reynolds number. *J. Fluid Mech.* **867**, 516–555.

LIU, Y., ZHANG, W., JIANG, Y. & YE, Z. 2016 A high-order finite volume method on unstructured grids using RBF reconstruction. *Comput. Maths Applics.* **72** (4), 1096–1117.

MALLIK, W., SCHETZ, J.A. & KAPANIA, R.K. 2018 Rapid transonic flutter analysis for aircraft conceptual design applications. *AIAA J.* **56** (6), 2389–2402.

MOISE, P., ZAUNER, M. & SANDHAM, N.D. 2024 Connecting transonic buffet with incompressible low-frequency oscillations on aerofoils. *J. Fluid Mech.* **981**, A23.

MOULIN, J. & MARQUET, O. 2021 Flow-induced instabilities of springs-mounted plates in viscous flows: a global stability approach. *Phys. Fluids* **33** (3), 034133.

OPGENOORD, M.M.J., DRELA, M. & WILLCOX, K.E. 2018 Physics-based low-order model for transonic flutter prediction. *AIAA J.* **56** (4), 1519–1531.

PALADINI, E., BENEDDINE, S., DANDOIS, J., SIPP, D. & ROBINET, J.-C. 2019a Transonic buffet instability: from two-dimensional airfoils to three-dimensional swept wings. *Phys. Rev. Fluids* **4** (10), 103906.

PALADINI, E., MARQUET, O., SIPP, D., ROBINET, J.-C. & DANDOIS, J. 2019b Various approaches to determine active regions in an unstable global mode: application to transonic buffet. *J. Fluid Mech.* **881**, 617–647.

PLANTE, F. Dandois, J., Beneddine, S., Laurendeau, É. & Sipp, D. 2021 Link between subsonic stall and transonic buffet on swept and unswept wings: from global stability analysis to nonlinear dynamics. *J. Fluid Mech.* **908**, A16.

POPLINGHER, L. & RAVEH, D.E. 2023a Comparative modal study of the two-dimensional and three-dimensional transonic shock buffet. *AIAA J.* **61** (1), 125–144.

POPLINGHER, L. & RAVEH, D.E. 2023b Stall flutter of the benchmark supercritical wing at high angles of attack. *AIAA SciTech 2023 Forum*.

POPLINGHER, L., RAVEH, D.E. & DOWELL, E.H. 2019 Modal analysis of transonic shock buffet on 2D airfoil. *AIAA J.* **57** (7), 2851–2866.

RAVEH, D.E. & DOWELL, E.H. 2011 Frequency lock-in phenomenon for oscillating airfoils in buffeting flows. *J. Fluids Struct.* **27** (1), 89–104.

RAVEH, D.E. & DOWELL, E.H. 2014 Aeroelastic responses of elastically suspended airfoil systems in transonic buffeting flows. *AIAA J.* **52** (5), 926–934.

RIVERA, J.A. JR., DANSBERRY, B.E., BENNETT, R.M., DURHAM, M.H. & SILVA, W.A. 1992 NACA 0012 benchmark model experimental flutter results with unsteadypressure distributions. In *33rd Structures, Structural Dynamics and Materials Conference*, p. 2396.

SARTOR, F., METTOT, C. & SIPP, D. 2015 Stability, receptivity, and sensitivity analyses of buffeting transonic flow over a profile. *AIAA J.* **53** (7), 1980–1993.

SCHEWE, G., MAI, H. & DIETZ, G. 2003 Nonlinear effects in transonic flutter with emphasis on manifestations of limit cycle oscillations. *J. Fluids Struct.* **18** (1), 3–22.

SCHUSTER, D.M., CHWALOWSKI, P., HEEG, J. & WIESEMAN, C.D. 2012 A summary of data and findings from the first aeroelastic prediction workshop. In *International Conference on Computational Fluid Dynamics*.

SHU, J.I., WANG, Y., KROLICK, W.C. & PANT, K. 2023 Parametric aeroelastic reduced-order model with state-consistence enforcement. *AIAA J.* **61** (3), 1109–1128.

SODA, A. & VOSS, R. 2005 Analysis of transonic aerodynamic interference in the wing-nacelle region for a generic transport aircraft. In *IFSAD*.

SPALART, P. & ALLMARAS, S. 1992 A one-equation turbulence model for aerodynamic flows. In *30th Aerospace Sciences Meeting and Exhibit*, p. 439.

WANG, G., MIAN, H.H., YE, Z.-Y. & LEE, J.-D. 2015 Improved point selection method for hybrid-unstructured mesh deformation using radial basis functions. *AIAA J.* **53** (4), 1016–1025.

YANG, Z., HUANG, R., LIU, H., ZHAO, Y. & HU, H. 2020 An improved nonlinear reduced-order modeling for transonic aeroelastic systems. *J. Fluids Struct.* **94**, 102926.

YAO, W. & JAIMAN, R.K. 2017 Model reduction and mechanism for the vortex-induced vibrations of bluff bodies. *J. Fluid Mech.* **827**, 357–393.

YATES, E.C. JR. 1987 AGARD standard aeroelastic configurations for dynamic response. candidate configuration I.-wing 445.6. *Tech. Rep.* 19880001820. Legacy CDMS.

ZHANG, W., GAO, C., LIU, Y., YE, Z. & JIANG, Y. 2015*a* The interaction between flutter and buffet in transonic flow. *Nonlinear Dyn.* **82**, 1851–1865.

ZHANG, W., JIANG, Y. & YE, Z. 2007 Two better loosely coupled solution algorithms of cfd based aeroelastic simulation. *Engng Applics. Comput. Fluid Mech.* **1** (4), 253–262.

ZHANG, W., LI, X., YE, Z. & JIANG, Y. 2015*b* Mechanism of frequency lock-in in vortex-induced vibrations at low Reynolds numbers. *J. Fluid Mech.* **783**, 72–102.

ZHANG, W., WANG, B., YE, Z. & QUAN, J. 2012 Efficient method for limit cycle flutter analysis based on nonlinear aerodynamic reduced-order models. *AIAA J.* **50** (5), 1019–1028.